Observation Impacts on the Mid-Atlantic Bight Front and Cross-Shelf Transport in 4D-Var Ocean State Estimates: Part II – The Pioneer Array

by

Julia Levin (julia@marine.rutgers.edu)[a], Hernan G. Arango (arango@marine.rutgers.edu)[a], Bruce Laughlin (blaughli@ucsc.edu)[b], Elias Hunter (hunter@marine.rutgers.edu)[a], John Wilkin (wilkin@marine.rutgers.edu)[a] and Andrew M. Moore (ammoore@ucsc.edu)[b*]

a: Department of Marine and Coastal Sciences, Rutgers, The State University of New Jersey, 71 Dudley Road, New Brunswick NJ 08901.
b: Department of Ocean Sciences, University of California, 1156 High Street, Santa Cruz CA 95062.

* Corresponding author: ammoore@ucsc.edu
Department of Ocean Sciences, University of California,
1156 High Street, Santa Cruz CA 95062.

Abstract

The Regional Ocean Modeling System (ROMS) 4-dimensional variational (4D-Var) data assimilation system was used to compute ocean state estimates of the Mid-Atlantic Bight (MAB). A three-level nested grid configuration was employed with horizontal resolution successively enhanced from 7 km down to 800 m at the innermost nest. This captures the dynamics on space- and time-scales ranging from the Gulf Stream western boundary current down to the rapidly evolving and energetic sub-mesoscale circulation. This is a companion study to Levin *et al.* (2020) which examined the overall impacts of the entire observing system on shelf-break exchange. This follow-on study specifically focusses on the impact of the *in situ* elements of the ocean observing system on the 4D-Var analyses. The particular focus here is on the Pioneer Array, a high-density observing system in the MAB designed to measure the multi-scale nature of shelf-break exchange processes. Building on Levin *et al.* (2020), it is found that the relative impact of observations from different components of the Pioneer Array depends on the scales of motion that are resolved by each nested grid. This is in apparent agreement with the linear theory of geostrophic adjustment despite the $O(1)$ Rossby number. The synergy between the observations from different observing platforms has also been quantified by comparing the observation impacts with the sensitivity of the 4D-Var analyses to changes in the observing array. It is found that while some observations do not have a significant *direct* impact on the analyses, they nevertheless provide essential information about the presence of circulation features, corroborating that measured by other sensors. Thus, the individual parts of the observing system can *borrow strength* from each other. Finally, the contribution of each component of the observing system to the expected error in the 4D-Var analyses was also quantified, where the critical role played by the Pioneer Array moorings in resolving the sub-mesoscale circulation is again highlighted.

Keywords: ROMS 4D-Var; Pioneer Array; Mid-Atlantic Bight; observation impact; observation sensitivity.

1 Introduction

This study is the companion of Levin *et al.* (2020; hereafter Part I) in which analyses of the circulation in the Mid-Atlantic Bight (MAB) were computed by combining ocean observations with an ocean model using state-of-the-art methods of data assimilation. The model used is the Regional Ocean Modeling System (ROMS) in conjunction with a 4-dimensional variational (4D-Var) data assimilation system. The model configuration comprises a hierarchy of three nested grids (Fig. 1) in which the resolution increases by a factor of 3 at each step, ranging from ~7 km down to ~0.8 km. Circulation features resolved span a broad spectrum of motions ranging from the Gulf Stream western boundary current, through an energetic mesoscale eddy field, all the way down to the $O(1)$ Rossby number flows that characterize the inhomogeneous, rapidly evolving, and ephemeral sub-mesoscale circulation. These circulation regimes all present considerable challenges for any data assimilation system.

The observing system comprises a combination of remote sensing platforms that provide surface measurements of temperature, sea level and ocean currents, as well as *in situ* platforms such as moorings, ships, surface drifters, profiling floats and piloted autonomous glider vehicles. An important and unique component of the MAB observing system is the Pioneer Array – one component of the U.S. National Science Foundation's (NSF) Ocean Observatories Initiative (OOI; Gawarkiewicz *et al.*, 2018). The Pioneer Array was designed to deliver sustained multi-scale observations in the vicinity of the MAB shelf break (see Fig. 1c) to investigate the processes that control the exchange of water masses between the continental shelf and the continental slope and associated biological and biogeochemical interactions. It is the Pioneer Array focus on shelf-break exchange processes that is of particular relevance to this study and the companion Part I.

In Part I, we explored the impact that observations from each element of the MAB and Gulf of Maine (GoM) observing systems have on different aspects of the 4D-Var state estimates. A main focus of Part I was on the performance of the 4D-Var system across the combination of nested grids, and the relative impact of the different observing platforms on cross-shelf exchange. In this companion study, we expand on the analyses of Part I and concentrate in particular on the impact of observations from the Pioneer Array on the 4D-Var analyses. While there are a variety of approaches that can be used to quantitatively assess the impact and information content of ocean observing systems (Oke *et al.* 2015a,b; Fujii *et al.*, 2019), the methodology used here is based on the adjoint approach of Langland and Baker (2004) that is used routinely at many operational weather forecasting centers to monitor the efficacy of global atmospheric observing systems (see http://ios.jcsda.org). A related and complementary diagnostic is observation sensitivity analysis which quantifies the sensitivity of ocean state estimates to changes in the observations and observing systems (Trémolet, 2008). There are many powerful extensions of this approach, which include computing estimates of the expected analysis errors (Moore *et al.*, 2012). In each case, the problem can be recast in such a way that the direct contribution or influence of each observation to the property under investigation can be computed. We present several applications of this approach here in relation to the Pioneer Array, focusing in some instances on the process of sub-mesoscale frontogenesis.

In this follow-on study to Part I, we explore in detail the impact of observations assimilated into a high resolution configuration of ROMS that resolves the sub-mesoscale circulation. There are few instances of 4D-Var at such high resolutions in the ocean, and this is an important exploration of the impact that different components of the observing system play in shaping the circulation estimates in this dynamical regime. As noted, a particular focus is the high density Pioneer Array. Another novel aspect of this study is quantification of the degree of synergy between different components of the observing system. Here we draw on the concept of *borrowing strength* from the field of statistics. The degree to which each component of the observing system is able to borrow strength is quantified here based on combining information from observation impact and observation sensitivity calculations. In addition, the extent to which different components of the Pioneer Array contribute to the reduction in the expected error of the 4D-Var analyses is also quantified. Perhaps rather surprisingly, it is also demonstrated that despite the high Rossby number regime of the resolved sub-mesoscale circulations, the relative impact of velocity and mass field observations with increasing model resolution can be explained using the linear theory of geostrophic adjustment.

A brief overview of the ROMS and 4D-Var configurations is presented in section 2. However, the reader is directed to Levin *et al.* (2019; hereafter, L19) and Part I for a more thorough explanation of the system. A description of the observations from the Pioneer Array and pertinent aspects of observation processing is presented in section 3. As described in Part I, the observation impact methodology used here involves targeted indices that highlight different aspects of the circulation that are of interest. The observation impact methodology is reviewed in section 4, along with the suite of circulation indexes that were employed. Section 5 presents an overview of the impact on each index of the observations from the various platforms that make up the Pioneer Array. In contrast, in section 6, we focus on some particular events, namely the interaction of a Gulf Stream ring with the continental shelf and the formation of a sub-mesoscale salinity front. The ideas of observation sensitivity are brought to bear in section 7 as a means of quantifying the synergy, within the 4D-Var algorithm, between observations from different components of the observing system. The observation sensitivity methodology is repurposed in section 8 to explore the contribution of each element of the Pioneer Array to the reduction in the expected error of the 4D-Var state estimates. The paper ends with a summary and conclusions in section 9.

2 Configuration of ROMS and 4D-Var

As discussed in Part I, the ROMS configuration used in this study comprises three nested grids, as illustrated in Fig. 1. Following Part I, the grid with the largest geographic extent will be referred to as G1 and has a horizontal resolution ~7 km and 40 terrain-following levels stretched so that the thickness of the surface-most layers is in the range 0.1-1.8 m and 0.1-3.4 m near the bottom over the continental shelf. The middle refined grid, hereafter G2, is centered on the Pioneer Array with a horizontal resolution of ~2.4 km, also with 40 terrain-following levels in the vertical. The innermost refined grid, hereafter G3, is likewise centered on the Pioneer Array with 40 levels in the vertical and ~0.8 km horizontal resolution. G1 was constrained at the open boundaries using data from the Mercator-Océan global analysis (Lellouche *et al.*, 2018) with temperature and salinity adjusted to remove seasonal bias compared to the local, regional climatology of Fleming (2016). In regular forward simulations, all three grids can be run using one- or two-way nesting. Harmonic tidal forcing (Mukai *et al.*, 2002) was added to the boundary SSH and depth-averaged velocity data of G1. Sea surface wind stress and heat and freshwater fluxes were derived on all three grids from 3-hourly National Centers for Environmental Prediction (NCEP) North American Mesoscale (NAM) forecast marine boundary layer conditions and standard bulk formulae of Fairall *et al.* (2003). Daily river in-flows were imposed at 22 discharge sites based on U.S. Geological Survey and Water Survey of Canada observations and a statistical model that adjusts for ungauged portions of the watershed (Lopez *et al.* 2020, Wilkin *et al.* 2018). Full details of the grid configurations can be found in Part I.

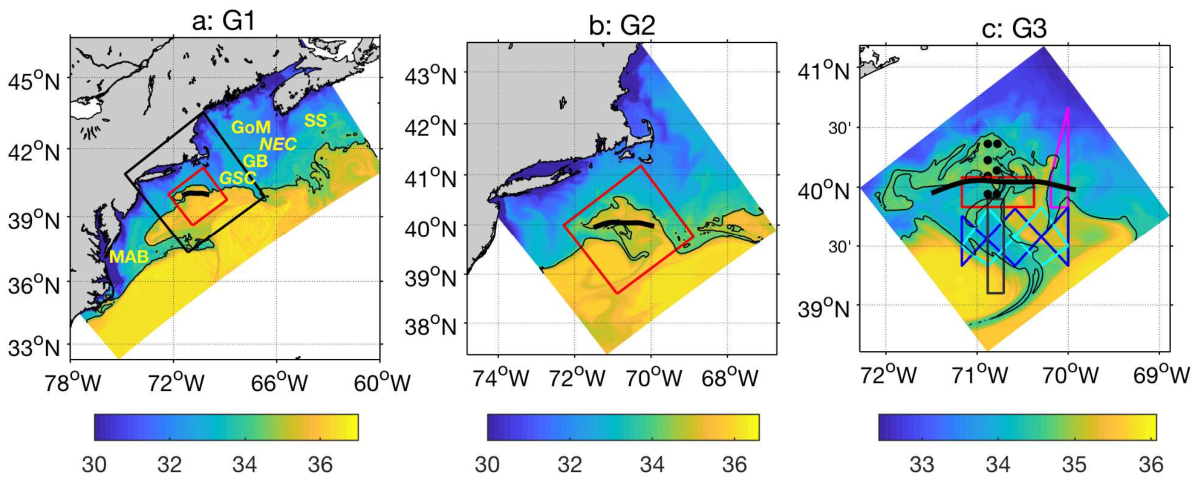

Figure 1: Snapshots of the sea surface salinity on 16 May 2014 from 4D-Var analyses on the three nested grids denoted (a) G1, (b) G2, and (c) G3. The 34.5 isohaline is often used as a proxy for the position of the Mid-Atlantic Bight shelf-break front and is highlighted in black in each figure. The location and extent of grids G2 (black rectangle) and G3 (red rectangle) are shown superimposed on G1 in (a). Also shown in (c) are the locations of the Pioneer moorings array (black dots), and the nominal Pioneer glider array (colored lined). The solid black line in each panel indicates the target section used to quantify shelf exchange. The locations of geographical features mentioned in the main text are also shown in (a): GoM=Gulf of Maine, GB=Georges Bank, GSC=Great South Channel, MAB-Mid-Atlantic Bight, NEC=North East Channel, SS=Scotian Shelf.

The configuration of the ROMS 4D-Var system is also described in detail in Part I, so only a summary of the important features will be presented here. Following the same notation as Part I, the ROMS state-vector will be denoted by $\boldsymbol{x}$ and comprises all of the ocean grid-point values of the ROMS prognostic variables, namely temperature (T), salinity (S), two components of horizontal velocity (u,v) and free-surface height (ζ). If $\boldsymbol{x}^b$ denotes the background state-vector and $\boldsymbol{x}^a$ is the 4D-Var analysis, then:

$$\boldsymbol{x}^a = \boldsymbol{x}^b + \boldsymbol{K}\left(\boldsymbol{y}^o - H(\boldsymbol{x}^b)\right) \quad (1)$$

where $\boldsymbol{y}^o$ denotes the vector of observations, H is the observation operator that maps from state-space to observation-space and includes the nonlinear model, and $\boldsymbol{K}$ is the Kalman gain matrix. In the application considered here, the dual form of 4D-Var was used (*e.g.* Courtier, 1997), in which case $\boldsymbol{K} = \boldsymbol{B}\boldsymbol{H}^T(\boldsymbol{H}\boldsymbol{B}\boldsymbol{H}^T + \boldsymbol{R})^{-1}$ where $\boldsymbol{B}$ and $\boldsymbol{R}$ are the background error and observation error covariance matrices respectively, and $\boldsymbol{H}$ represents the tangent linearization of the observation operator H. In 4D-Var $\boldsymbol{H}$ includes the tangent linearization of the nonlinear model and $\boldsymbol{H}^T$ includes the adjoint model. The inverse of the stabilized representer matrix $(\boldsymbol{HBH}^T + \boldsymbol{R})^{-1}$ is evaluated iteratively using a conjugate gradient descent algorithm, as described by Gürol *et al.* (2014). This procedure is equivalent to a truncated Gauss-Newton method, which takes the form of a sequence of linear minimization problems. Each such sequence is solved via several inner-loop iterations, while each separate sequence constitutes an outer-loop. In the 4D-Var calculations considered here, two outer-loops and seven inner-loops were used on all three grids, and a summary of the data assimilated is presented in Table 1.

For G1 and G2, the period Jan 2014 - Dec 2017 was considered, while for G3, the shorter interval Jan 2014 – Dec 2015 was used because of the substantial computational effort required for this grid. The data assimilation strategy employed was as follows: (1) Observations were first assimilated into G1 for the full 2014-17 period using a 3-day assimilation window, and treating the model initial conditions, surface forcing (all components), and open boundary conditions as control variables. The background state estimate for each 3-day window was taken to be the analysis at the end of the previous cycle. (2) Step (1) was then repeated for grid G2, using the 4D-Var analyses from each cycle of G1 as the background open boundary conditions for each 4D-Var cycle of G2. As in G1, the initial conditions, surface forcing, and open boundary conditions were all adjusted during each 4D-Var cycle. (3) Step (2) was then repeated for grid G3, using the 4D-Var analyses from each cycle of G2 as the background open boundary conditions for each 4D-Var cycle of G3. In this case, the 4D-Var window was reduced to 1-day, and only the initial conditions and open boundary conditions were adjusted during each 4D-Var cycle.

Type & platform	**Source**	**Sampling rate and resolution**	**Super-obs averaging[1]**			**Obs error**
			G1	**G2**	**G3**	
AVHRR IR SST	MARACOOS.org & NOAA Coastwatch	4 passes per day, 1 km	3 h	3 h	3 h	σ_b
GOES IR SST	NOAA Coastwatch	Hourly, 6 km	3 h	3 h	3 h	$2\sigma_b$
AMSR2, TRMM and WindSat microwave SST	NASA JPL PO.DAAC	Daily, 15 km	3 h	3 h	3 h	$1.25\sigma_b$
SSH Jason, AltiKa, CryoSat	RADS, TU Delft	~1 pass daily, ~7 km				0.04 m
in situ T, S: NDBC buoys, Argo floats, XBT, surface drifters	Met Office En4.2	Variable[2]	Std.lev[2]	Std.lev[2]	Std.lev[2]	$0.25\sigma_b\sigma_o/\sigma_{max}$[3]
Surface velocity: HF-radar	MARACOOS.org	Hourly, 6 km	24 km	24 km	24 km	$0.5\sigma_b$
in situ T,S: MARACOOS gliders	IOOS Glider DAC	Variable[2]	2 h, Std.lev[2]	1 h, Std.lev[2]	0.33 h, Std.lev[2]	$0.25\sigma_b\sigma_o/\sigma_{max}$[3]
in situ T,S: Gulf of Maine	NERACOOS.org[4]	Hourly, 10 buoys				σ_b
in situ u,v: Gulf of Maine		Hourly, 9 buoys[1]				$0.5\sigma_b$

in situ T,S: Pioneer moorings	NSF Ocean Observatories Initiative[7]	~3 h profiles, 7 moorings[5] ~60% data availability[6]	2 h, Std.lev[2]	1 h, Std.lev[2]	0.33 h, Std.lev[2]	$0.25\sigma_b\sigma_o/\sigma_{max}$[3]
in situ T,S: Pioneer gliders		Variable[2] ~4 h, ~4 km	2 h, Std.lev[2]	1 h, Std.lev[2]	0.33 h, Std.lev[2]	$0.25\sigma_b\sigma_o/\sigma_{max}$[3]
in situ u,v: Pioneer moorings		30 min, ~75% data availability[6]	Std.lev[2]	Std.lev[2]	Std.lev[2]	$0.5\sigma_b$

Table 1: A summary of the observational data assimilated into ROMS during 2014–2017, the procedure for forming super observations, and the observation errors assigned to each observation type. The final column, σ_o and σ_b denote the standard deviation of observation errors and background errors respectively, the formulae given are the scaling relationships used for the indicated observation types. The superscripts provide additional information. 1: All data that were sampled at a horizontal resolution higher than that of the model were formed into super observations at the resolution of the ROMS grid unless otherwise indicated. 2: Profile data were binned in the vertical using the WOD atlas standard depths (Boyer *et al.*, 2009). 3: Here σ is the standard deviation of all observations that fall within a vertical bin (see comment 1) and σ_{max} is the maximum value of all σ in a vertical profile. 4: NERACOOS = North East Regional Association Coastal Ocean Observing System. 5: Moorings 2 and 4 deployed November 2017. 6: Average over 2014-2017, see also Fig. 2. 7: Data downloaded from NSF OOI Data Portal http://ooinet.oceanobservatories.org and aggregated by platform at http://www.myroms.org:8080/erddap/info. From Part I.

As discussed in Part I and described in Moore *et al.* (2011a), the background error covariance ***B*** matrix was modeled following the diffusion operator approach of Weaver and Courtier (2001). The decorrelation length scales assumed in ***B*** for errors in each control variable are listed in Table 2, and these parameter choices are discussed in L19.

State variable	**Horizontal decorrelation scale (km) (G1|G2|G3)**	**Background quality control parameter γ (G1|G2|G3)**
SSH	40 | 14 | 5	5 | 5 | ∞
Velocity	40 | 14 | 5	1.5 | 1.5 | ∞
Temperature	15 | 14 | 5	6 | 6 | 6
Salinity	15 | 14 | 5	12 | 12 | 12
Surface forcing	100 | 100 | -	-

Table 2: A summary of the decorrelation scales assumed for background errors in each control variable on all three grids. The vertical decorrelation length scale for all state variables of the initial conditions and open boundary conditions was chosen to be 10 m. In the case of the surface forcing, the same horizontal decorrelation lengths were imposed on all fields. The parameter γ used for the background quality control rejection criteria is also indicated: $\gamma = \infty$ indicates that no background quality control check was applied to these data. A dash in any column indicates that the parameter is not applicable.

The observation error covariance matrix ***R*** was assumed to be a diagonal matrix, and Table 1 summarizes the errors and uncertainties that were assigned to measurements from each observing platform. As discussed in L19, these errors reflect a combination of measurement error and errors of representativeness (*i.e.*, uncertainties associated with the ability of the model grid to resolve all of the processes that are captured by the observations). Quality control was performed during each 4D-Var cycle, following Andersson and Järvinen (1999), where the innovation d_i associated with each observation is compared to the standard error based on the assumed standard deviations of the background (σ_b) and observation (σ_o) errors. If $d_i^2 > \gamma^2(\sigma_b^2 + \sigma_o^2)$, then the observation is rejected and not included in the analysis. The threshold parameter γ is dependent on the type of observation and is given in Table 2 for the analyses on each grid considered here.

The performance of the 4D-Var system on all three grids is discussed in detail by L19 and in Part I, therefore no particulars will be given here. Suffice to say that the data assimilation system performs well on all three grids across the range of circulation length scales resolved and is able to fit the model solution to the observations reliably.

3 The Pioneer Array

An important component of the observing system in the MAB is the U.S. National Science Foundation (NSF) Ocean Observatories Initiative (OOI) Pioneer Array, and the impact of the observations from this array on the 4D-Var ocean circulation estimates will be the focus of this study. The Pioneer Array comprises seven permanent moorings (Fig. 2) that straddle the continental shelf break where measurements of temperature and salinity from profiling CTD and velocity from ADCP are made through almost the full depth of the water column (ranging from ~130 m to ~450 m). The CTD sample rate gives centimeter scale vertical resolution; ADCP velocity is reported in 4-m or 8-m bins at shallow and deep sites, respectively. The mooring observations are complemented by multiple gliders that repeatedly sample along the nominal tracks shown in Fig. 2, although the actual paths followed are subject to the vagaries of remotely piloting slowly moving buoyancy driven gliders in a turbulent ocean.

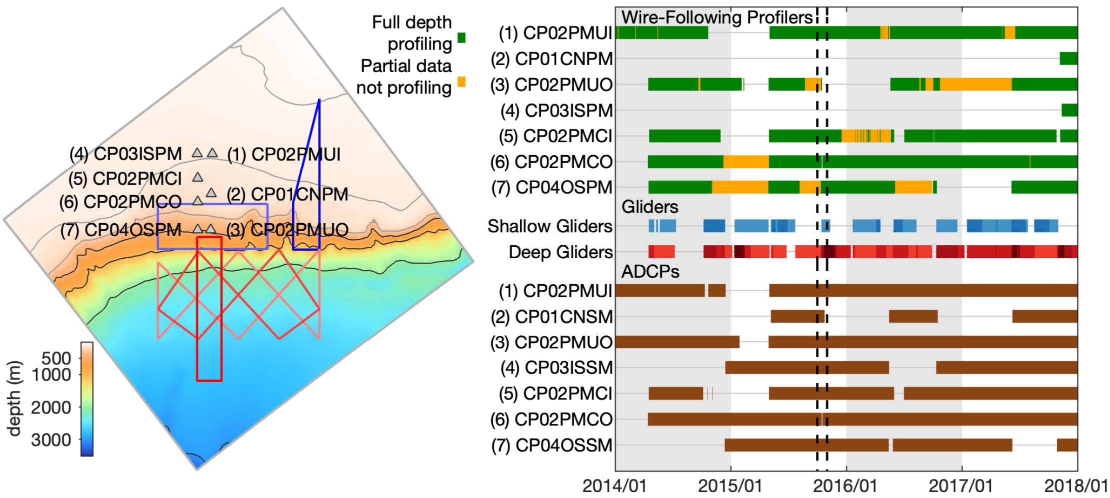

Figure 2: Map (left) shows domain and bathymetry of grid G3, and the observing assets that comprise the U.S. National Science Foundation (NSF) Ocean Observatories Initiative (OOI) Pioneer Array. Symbols show fixed moorings, with numbers 1 to 7 used in text to denote individual moorings, and their 8-character OOI platform names. Blue and red lines on the map are the nominal Pioneer repeat glider tracks. Time bars (right) indicate when in 2014-2017 instruments returned data that were used here. Wire-following profilers are green when successfully acquiring full depth range data, but yellow when stuck and returning data from a fixed depth only. Blue and red bars

indicate data from shallow and deep, respectively, profiling gliders; bars are darker when multiple gliders are operating, showing at most 2 shallow and 4 deep gliders operating simultaneously in 2014-2017. Brown bars show ADCP current-meters. Vertical dashed lines indicate the October 2015 period that is the focus of section 6.

Figure 2 shows when in 2014-2017 the various observing assets were returning data. On average, data from CTD profilers were available about 60% of the time (not including the late-2017 deployments at moorings 2 and 4) and for ADCP about 75% of the time. Note that there was a protracted period of low data return across the array in early 2015. Powered Autonomous Underwater Vehicle (AUV) deployments are also a component of the Pioneer Array design, but none took place during the 2014-2017 period considered here.

In addition to Pioneer, the other observations noted in Table 1 were assimilated if they fell into the domains spanned by the respective nested grids. As demonstrated in sequel, observations from remote sensing and other *in situ* platforms lend support to the measurements collected by the Pioneer Array, and vice versa.

4 Observation Impacts Methodology and Indexes

The procedure used to evaluate the impact of the observations on each 4D-Var analysis follows the method originally developed by Langland and Baker (2004). The implementation in ROMS is described in some detail by L19 and in Part I, so again only a summary of the essential points will be presented here.

The impact of the observations on the analysis $\boldsymbol{x}^a$ is quantified in terms of the influence that they have on an index, $I(\boldsymbol{x})$, that isolates some aspect of the circulation that is of interest. Following Langland and Baker (2004), the change in I due to assimilating the observations $\boldsymbol{y}^o$ is given by $\Delta I = I(\boldsymbol{x}^a) - I(\boldsymbol{x}^b)$, which to 1st-order, can be expressed as $\Delta I \approx \left(\boldsymbol{y}^o - H(\boldsymbol{x}^b)\right)^T \boldsymbol{K}^T(\partial I/\partial \boldsymbol{x})|_{\boldsymbol{x}^b}$ where $(\partial I/\partial \boldsymbol{x})|_{\boldsymbol{x}^b}$ is a vector and represents the derivative of I with respect to each element of $\boldsymbol{x}$ evaluated using the background $\boldsymbol{x}^b$. As described in Part I, the transposed Kalman gain matrix can be reconstructed using the archived conjugate gradient descent vectors from each 4D-Var assimilation cycle. It should be clear that ΔI is given by the dot-product of the innovation vector $\boldsymbol{d} = \left(\boldsymbol{y}^o - H(\boldsymbol{x}^b)\right)$ and the vector $\boldsymbol{g} = \boldsymbol{K}^T(\partial I/\partial \boldsymbol{x})|_{\boldsymbol{x}^b}$, which quantifies the impact of the observations on ΔI. Since each element of $\boldsymbol{d}$ is uniquely associated with an individual observation, so then are the corresponding elements of $\boldsymbol{g}$ such that the product $d_i g_i$ represents the contribution (aka *impact*) of the i^{th} observation to ΔI.

Following Part I, the chosen indexes $I(\boldsymbol{x})$ target variations in the position of the MAB shelf-break front and the strength of the associated stratification and cross-shelf transport in the vicinity of the Pioneer Array. Specifically, we consider five indexes:

$$I_u = \int_{s_1}^{s_2} \int_h^0 (\bar{u}_n - \tilde{u}_n) dz ds \quad (2)$$

$$I_{uT} = \rho_o c_p A^{-1} \int_{s_1}^{s_2} \int_h^0 (\bar{u}_n - \tilde{u}_n)(\bar{T} - \tilde{T}) dz ds \quad (3)$$

$$I_{uS} = 10^{-3}\rho_o A^{-1} \int_{s_1}^{s_2} \int_h^0 (\bar{u}_n - \tilde{u}_n)(\bar{S} - \tilde{S}) dz ds \quad (4)$$

$$I_f = \int_{\xi_1}^{\xi_2} \big(\eta(\xi) - \eta^r(\xi)\big) d\xi \quad (5)$$

$$I_e = V^{-1} \iint g \int_D^{\zeta} (\bar{\rho} - \rho) z dz dA. \quad (6)$$

The indexes I_u, I_{uT}, and I_{uS} target the volume, heat, and salt transport respectively across a section of the h=200 m isobath defined by the integral $\int_{s_1}^{s_s} \cdots ds$, which is nominally identified as the location of the continental shelf-break. The location of the vertical section chosen is indicated in each panel of Fig. 1 and cuts through the middle of the Pioneer Array. In (2) - (4), u_n corresponds to the component of the velocity that is locally normal to the section s, an over-bar denotes the time average over each assimilation cycle, the tilde represents the mean seasonal cycle, and A is the area of the cross-section. Each index was evaluated using a finite difference approximation consistent with the appropriate model grid.

The index I_f in (5) targets the location where the 34.5 isohaline intercepts the bathymetry, a traditional proxy for the foot of the MAB shelf-break front (Beardsley *et al.*, 1985; Linder and Gawarkiewicz, 1998). In (5), (ξ, η) represent the local cartesian coordinates position of the foot of the front averaged in time over the particular 4D-Var cycle, and $\eta^r(\xi)$ is a reference line chosen to be the seasonally varying climatological position of the front. It follows then that the area defined by I_f is proportional to the departure of the front position from its seasonal mean. The endpoints ξ_1 and ξ_2 of the integral concide with the east-west limits of Pioneer Array glider operations (Fig. 1).

Following Simpson and Bowers (1981), the index I_e in (6) is the potential energy per unit volume that would be gained were the upper part of the water column to become vertically mixed, and is hence a measure of the strength of the vertical stratification. In (6) ρ and $\bar{\rho}$ are respectively the *in situ* and vertically averaged density, both averaged over the assimilation window, D is a chosen depth, ζ is the free-surface displacement, and the area integral is performed over the Pioneer Array glider domain (*cf* Figs. 1c). The depth D was chosen to be the average depth of the front foot across the Pioneer Array glider domain. In (6), V represents the volume encompassed by the integrals with the result that I_e represents the energy per unit volume (J m^{-3}) that is required to completely vertically mix the upper D meters of the water column within the Pioneer Array glider operations box (*cf* the red rectangle in Fig. 6).

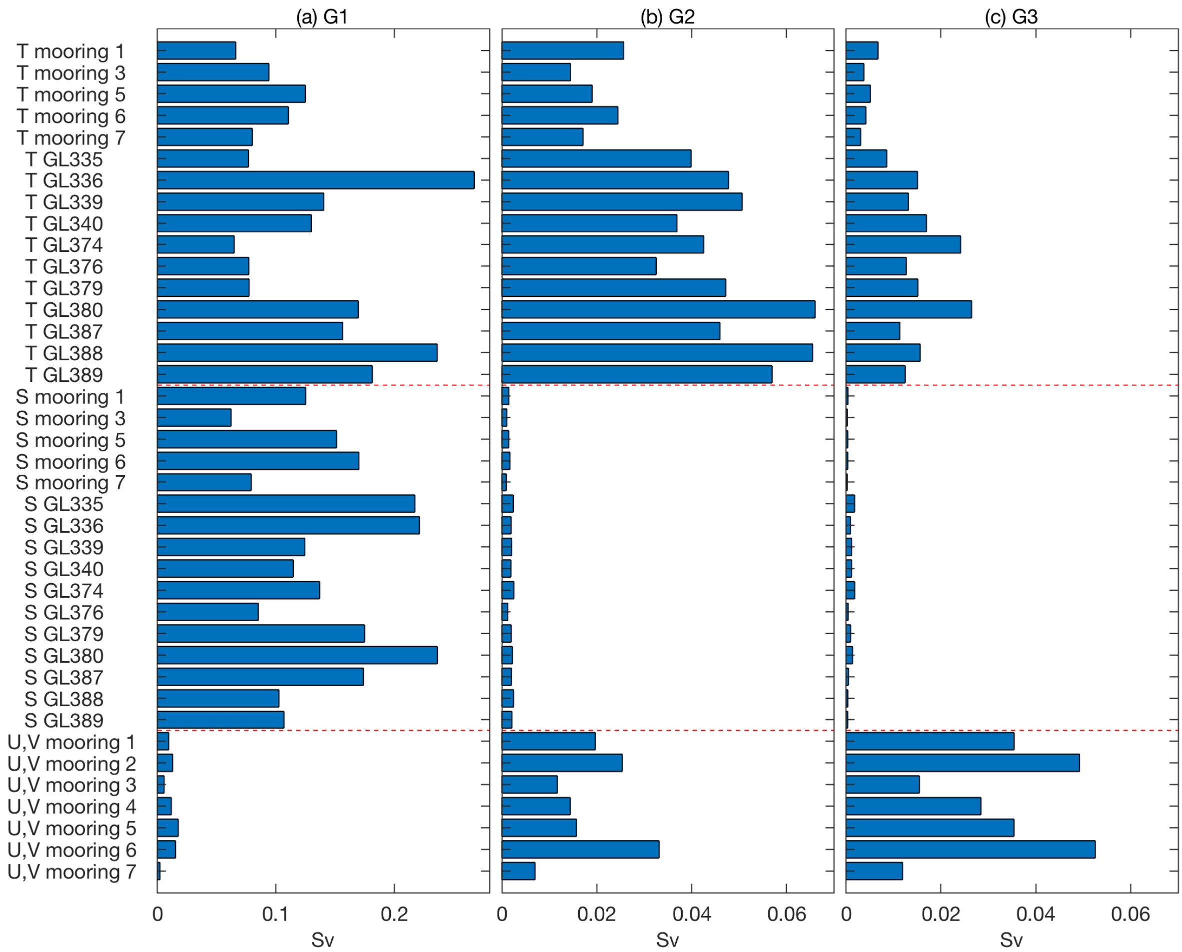

Figure 3: RMS impacts of individual observing system components of the Pioneer Array on I_u for all 4D-Var cycles during 2014 and 2015 for (a) G1, (b) G2, and (c) G3. The observation impacts are grouped based on observation type (*i.e.*, temperature (T), salinity (S), velocity (U,V)), and the horizontal dashed red lines separate the bar charts associated with each observation type. The locations of the numbered moorings are indicated in Fig. 2, while the gliders (GL) are referred to by their OOI 5-character identifiers.

5 Pioneer Array Observation Impacts

The relative impact of the various platforms that comprise the entire regional observing system (Table 1) on the target indexes introduced in section 4 is presented in Part I. L19 have also considered, in some detail, the impact of each remote sensing platform on a subset of the same indexes on the 4D-Var analyses of G1. In this section, we will focus attention on the impact of the observations from the different instruments and platforms that make up the Pioneer Array.

As noted in section 2, the period Jan 2014 – Dec 2015 is common to the 4D-Var analyses computed on all three grids. With this in mind, Fig. 3 shows the root mean square (RMS) impact on I_u averaged over *all* 2014-2015 4D-Var analysis cycles of the individual Pioneer Array moorings and gliders. The mooring numbering used in Fig. 3 is as indicated in Fig. 2, which also gives the 8-character designations used by OOI. The gliders are referred to by their OOI 5-character identifiers. The impact of the temperature, salinity, and velocity measurements from each mooring are reported separately, as are the impacts of the temperature and salinity observations from each glider.

As discussed in Part I, the parameters used to compute the observation error covariance matrix, $\boldsymbol{R}$, and background error covariance matrix, $\boldsymbol{B}$, are not the same on the three grids. Some of the differences in $\boldsymbol{R}$ are reflected in the observation impacts. The observation error standard deviations, σ_o, assumed for *in situ* temperature observations are similar across all three grids and range from ~0.6°C on G1 to ~0.4°C on G2 and G3. However, as noted in Part I, *a posteriori* analysis of the innovation statistics, following the diagnostics described by Desroziers *et al.* (2005), suggests that σ_o should be closer to ~1°C. The *a priori* values of σ_o for *in situ* salinity observations were assumed to ~0.2 on G1, while the *a posteriori* innovation statistics indicate that ~0.4 is a more appropriate choice. A value of $\sigma_o = 0.4$ was therefore used for the *in situ* salinity observation errors in both G2 and G3. For velocity measurements, the σ_o on G1 was assumed to be ~0.6 ms^{-1} for HF radar surface current estimates and ~0.3 ms^{-1} for moorings. These values were adjusted downwards to ~0.1 ms^{-1} for HF radar observations and ~0.04 ms^{-1} for moorings for both G2 and G3 which are more in line with the *a posteriori* innovation statistics. The high computational cost of 4D-Var precludes a more detailed and controlled suite of experiments, where, for example, the parameters of the data assimilation system are varied independently across the three grids. Therefore, we must draw on what we have, although the variations in the level of errors across the different grids provide an indication of their control on the impacts.

With this in mind, Fig. 3a shows that by-and-large, it is temperature and salinity observations from the glider platforms that have the largest impact on I_u of the G1 analyses. On the other hand, the velocity observations from the Pioneer Array moorings have a relatively low impact on G1 because the ~7 km horizontal resolution of this grid cannot adequately resolve the mooring array. On G2, Fig. 3b shows that temperature observations from the gliders still exert a significant influence on I_u. However, the impact of salinity observations on G2 is much reduced compared to G1, mainly because, as noted above, σ_o for salinity was increased on G2 compared to G1. The observation error statistics assumed for salinity on G2 and G3 are similar, so the impact of these data is alike on both grids. However, Fig. 3b indicates that velocity observations from the Pioneer Array moorings now play a more dominant role in shaping the circulation estimates on G2. Some of the difference between the impact of velocity observations on G1 and G2 can be attributed to the reduction in σ_o noted above. Even though the σ_o for the mooring data on G3 are similar to those on G2, the impact of the velocity observations is higher still on G3 (Fig. 3c). In this case, the mooring velocity observations exert more control over the transport increments because the resolution of G3 is high enough to resolve some of the sub-mesoscale circulation features that are captured by the moorings (see section 6 for more details).

The relative impact of the various Pioneer observing platforms on I_{uT}, I_{uS}, I_f, and I_e is qualitatively similar to that for I_u (not shown).

Time series of the 2015 increments ΔI for all five indexes on G3 are shown in Fig. 4. In each case, the contribution of the different observation types to the increment during each 4D-Var cycle is also indicated. The dominant impact of velocity observations on all of the indexes is very apparent. Figure 4 also shows that satellite SST and *in situ* temperature measurements also have a significant influence, the latter almost exclusively associated with Pioneer gliders and moorings. The impact of altimetry is negligible on G3 since there are very few satellite overpasses so is not shown. However, as shown in Part I, satellite SSH does exert significant control on each index in G1 and G2.

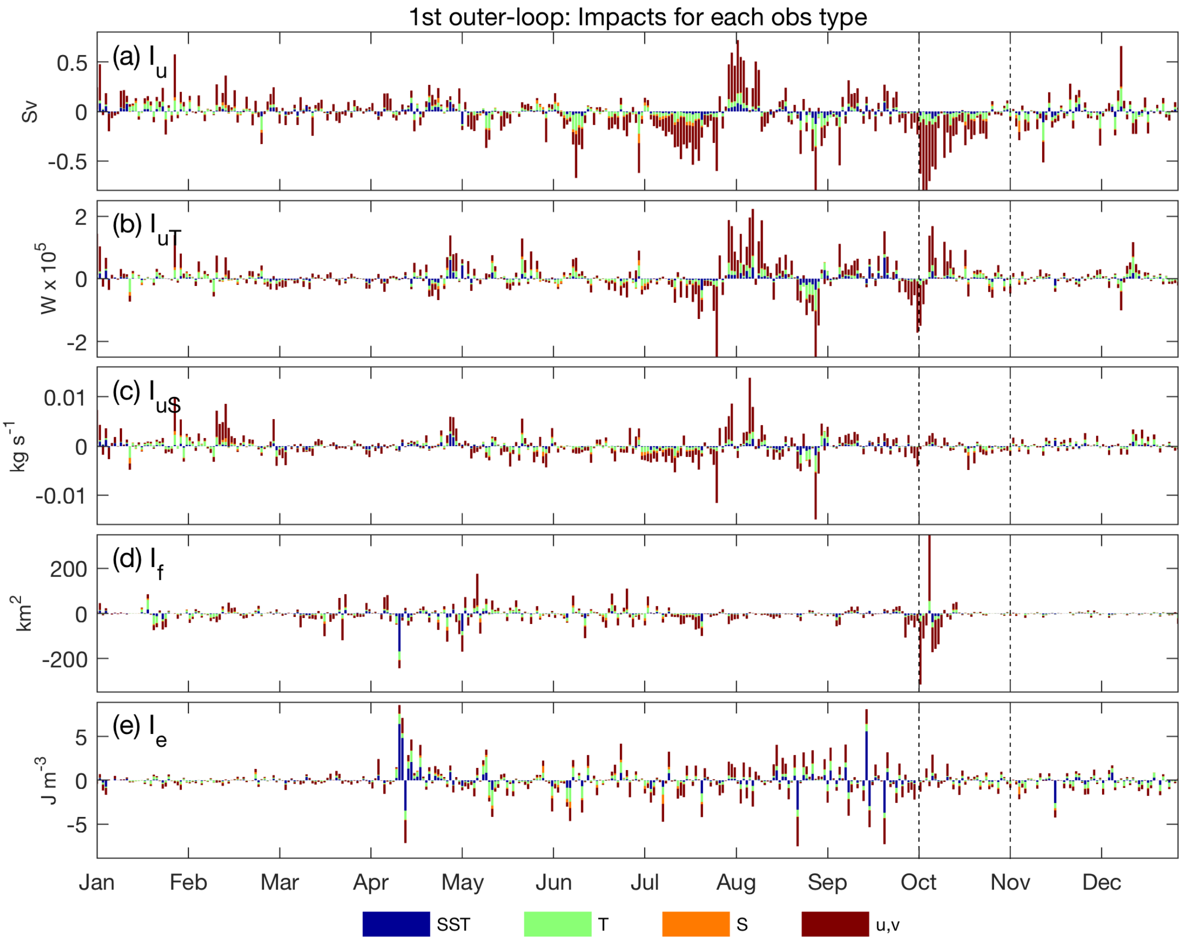

Figure 4: Time series of the 2015 G3 4D-Var increments in (a) I_u, (b) I_{uT}, (c) I_{uS}, (d) I_f, and (e) I_e. The colors indicate the contribution (aka "impact") that observations of each type make to the total increments. The vertical dashed lines correspond to the period considered in detail in section 6. The SSH impacts are negligible and are not shown.

Figure 4 reveals that the increments in several of the indexes are larger during the second half of 2015. In particular, there are some periods of prolonged, coherent increments such as July-August and October indicating that the data were likely prompting the 4D-Var system to make more substantial changes to the state estimates during these periods than was typical. We will focus on the latter October 2015 period in the next section and explore in some detail the circulation environment during that time.

6 October 2015 Case Study

6.1 Transport Increments

The increments in volume transport, ΔI_u, and heat transport, ΔI_{uT}, in Figs. 4a and 4b indicate that during October 2015, the 4D-Var system made coherent and sustained changes in cross-shelf transport for several weeks. Similarly, there were significant movements in the MAB front during this same period, as indicated by ΔI_f. In this section, we will focus on this period and explore in detail the impact of the individual assets of the Pioneer Array. While Fig. 4 shows the index increments only for G3, the increments are broadly consistent across all three grids. This is illustrated in Fig. 5, which shows time series of the *total* volume transport $I_{\bar{u}} = \int_{s_1}^{s_2} \int_h^0 \bar{u}_n dzds$ during October 2015. The total transport $I_{\bar{u}}$ is displayed instead of the transport I_u given by (2) to remove any differences between the seasonal variations $\tilde{u}_n$ on the three grids. Figure 5 also shows time series of $\Delta I_{\bar{u}} = \Delta I_u$ for October 2015 for each grid. On all three grids, the transport $I_{\bar{u}}$ is positive indicating onshore flow, which 4D-Var acts to reduce during most cycles. The increments on G2 and G3 are generally consistent with each other, although they are somewhat smaller in G2. (The time resolution differs because G3 uses a 1-day analysis interval, whereas in G1 and G2 it is 3 days.) On G1, ΔI_u is more variable and onshore during the period 8-13 October, whereas G2 and G3 indicate offshore increments during this time. In the case of G1, observations that are remote from the target section exert a significant influence on all of the indexes, as demonstrated in L19 and Part I, particularly observations in the vicinity of the Gulf Stream front and Georges Bank. These influences are absent from G2 and G3 due to their smaller geographical extent, which is one of the primary reasons why ΔI_u is not entirely consistent between G1 and grids G2 and G3. The other indexes display a similar behavior across the three grids (not shown).

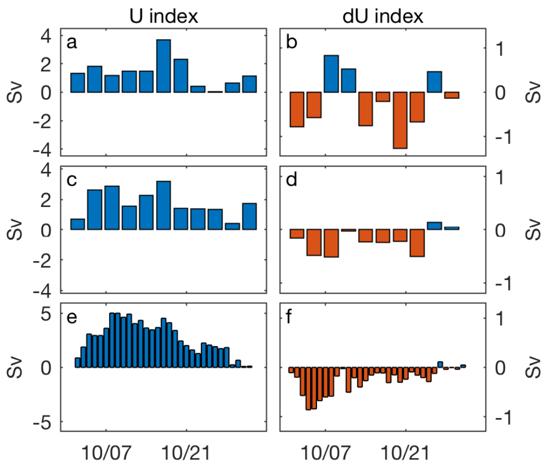

Figure 5: Time series of $I_{\bar{u}}$ (left) and ΔI_u (right) for each 4D-Var data assimilation cycle during October 2015 for grids (a,b) G1, (c,d) G2, and (e,f) G3.

6.2 The Sub-Mesoscale Environment

To illustrate the circulation environment that develops during the focus period, Figs. 6 and 7 show the 4D-Var surface circulation estimates for G2 and G3 on 8 October when a warm-core ring is impinging on the continental shelf in the western vicinity of the Pioneer Array. The ring entered the region in early September from the east having coalesced into a coherent anticyclonic feature from a modest positive geopotential anomaly shed from the Gulf Stream in August. The intrusion of warm, saline Gulf Stream waters onto the shelf north and east of the ring are apparent in both G2 and G3. Figures 6c and 7c show the relative vorticity of the vertically averaged velocity on the same day normalized by the Coriolis parameter (*i.e.*, the local Rossby number). A region of uniform negative vorticity identifies the center of the Gulf Stream ring, which is flanked by filamentous vorticity features; small scale structures are ubiquitous on the shelf. In both grids, the vorticity color bar has been saturated to highlight the complex circulation structure. However, the local Rossby number is generally significantly larger than one over much of the domain indicative of a non-linear circulation environment.

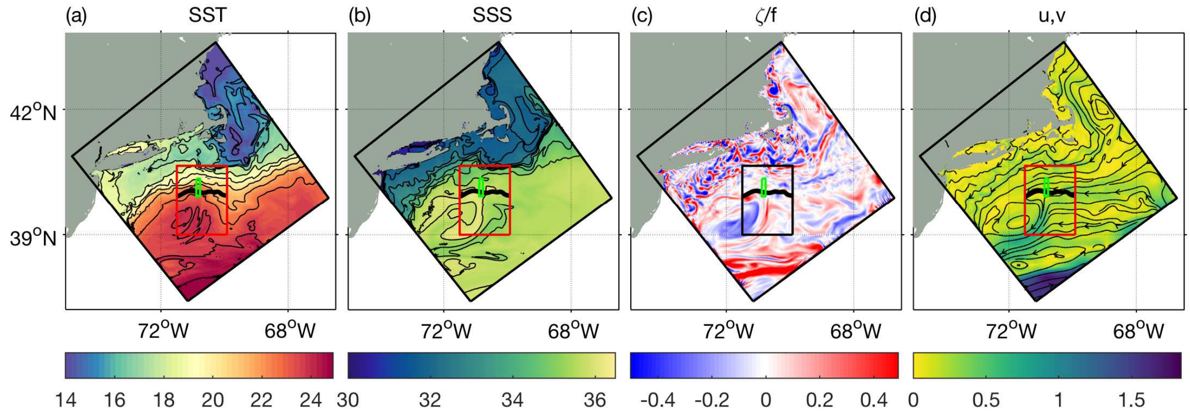

Figure 6: The 8 October daily average 4D-Var analysis fields on G2 of (a) SST, (b) sea surface salinity (SSS), (c) vertically averaged relative vorticity normalized by f, and (d) surface current speed (color) and streamlines. The location of the Pioneer mooring array (green rectangle) and the nominal extent of the Pioneer glider sampling region (red rectangle in (a), (b), (d) and black rectangle in (c)) is also shown. The target section used to quantify shelf exchange is indicated by the heavy black line.

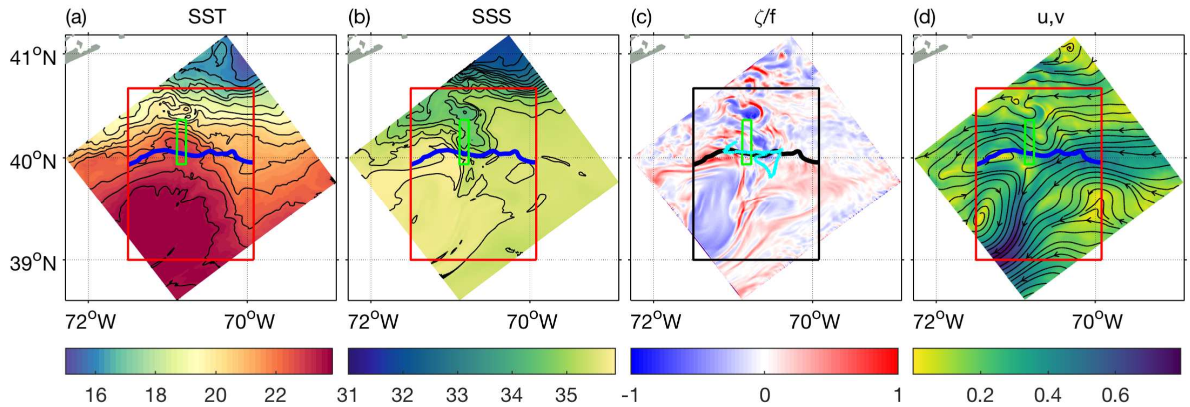

Figure 7: Same as Fig. 6 but for G3. The cyan line in (c) shows the path of glider GL380 during October 2015. The target section used to quantify shelf exchange is indicated by the heavy black line in (c) and heavy blue line in (a), (b) and (d).

In the case of G3, Fig. 7c reveals numerous sub-mesoscale fronts, jets, and filaments in the vicinity of the Pioneer Array. Figure 7d shows that at the western end of the target section and near the offshore Pioneer moorings, a complex pattern of confluent and diffluent flows (~0.3-0.4 m s^{-1}) has developed, which promotes frontogenesis in this region and acts to draw out the vorticity filaments that are so evident in Fig. 7c. Indeed, closer inspection of Fig. 7b reveals that at the boundary of the mesoscale circulation features in this same region, a filament of less saline shelf water is being drawn offshore right through the Pioneer mooring array and across the target section. Adjacent to and west of the low salinity tongue, more saline Gulf Stream waters are being drawn onto the shelf and a front forms, as evidenced by the sharp surface salinity gradient.

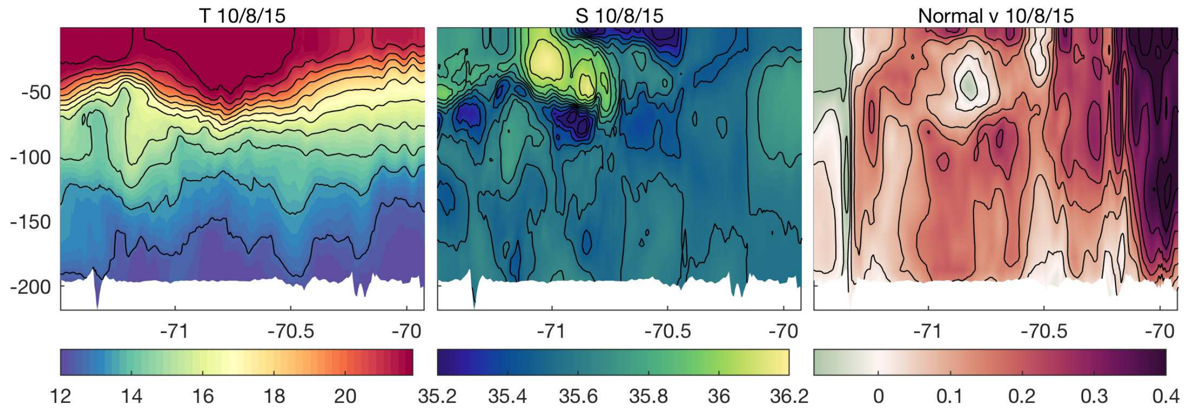

Figure 8: Vertical sections along the 200m isobath target section (see Fig. 7) on 8 October 2015 from the G3 4D-Var analysis of (a) temperature, (b) salinity, and (c) the normal component of velocity.

The complexity of the circulation at this time is further apparent in Fig. 8, which shows vertical sections on 8 October of the temperature, salinity, and the normal component of velocity along the target section following the 200-m isobath. Even though the net transport is onshore at this time (*cf.* Fig. 5e), Fig. 8c indicates that there are variations in the flow along the section and at depth. The signature of the mesoscale eddy field is evident in the thermocline structure in Fig. 8a, while Fig. 8b shows that the tongue of fresher water that is drawn off the continental shelf between 71°W and 70.5°W (*cf.* Fig. 7b) is confined mainly to the upper 10-20 m and is associated with a complicated interleaving salinity structure and stacked flows of alternating direction and strength which contribute to the formation of the aforementioned salinity front.

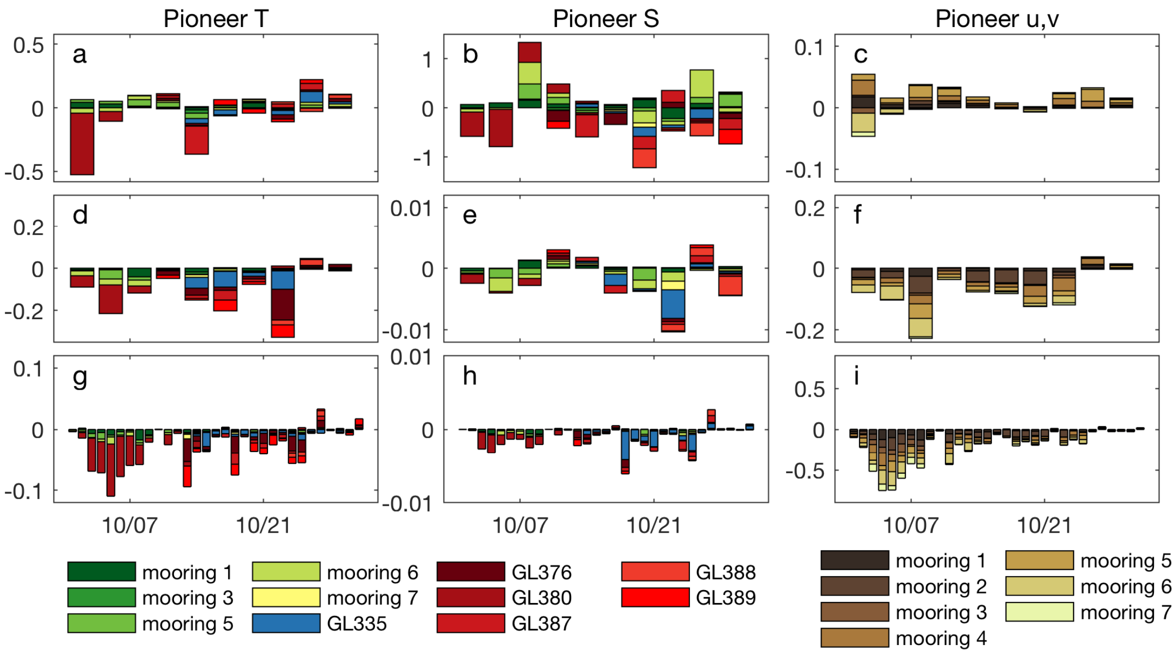

Figure 9: Time series of the impact of Pioneer temperature, salinity, and velocity observations on ΔI_u for each 4D-Var data assimilation cycle during October 2015 for (a,b,c) G1, (d,e,f) G2, and (g,h,i) G3. The different colored segments indicate the contribution of each observation platform. The key for the *T* and *S* platforms is shown to the left, while the key for the velocity observations is shown to the right. In the case of the gliders (GL), shallow gliders are indicated by blue while deep gliders are indicated by different shades of red.

6.3 Pioneer Array Observation Impacts

Time series of the contributions of the Pioneer Array temperature, salinity, and velocity observations to the cross-shelf volume transport increments ΔI_u are shown in Fig. 9 for all three grids. We caution against making particular inferences regarding how the impact of individual platforms varies during the month because of changes in instrument operations (Fig. 2), including glider recovery and deployments such that the 6 gliders noted in Fig. 9 represent collectively only 3 months of data. What Fig. 9 does show clearly, once again, is how the impact of the *in situ* temperature and salinity measurements from the various glider platforms diminishes as the horizontal grid resolution increases. Conversely, as noted earlier, the impact of the *in situ* velocity observations from the moorings increases from G1 to G3. The results of Fig. 9 are generally consistent for the other indexes also, and we will postpone a broader discussion of these findings until section 7.

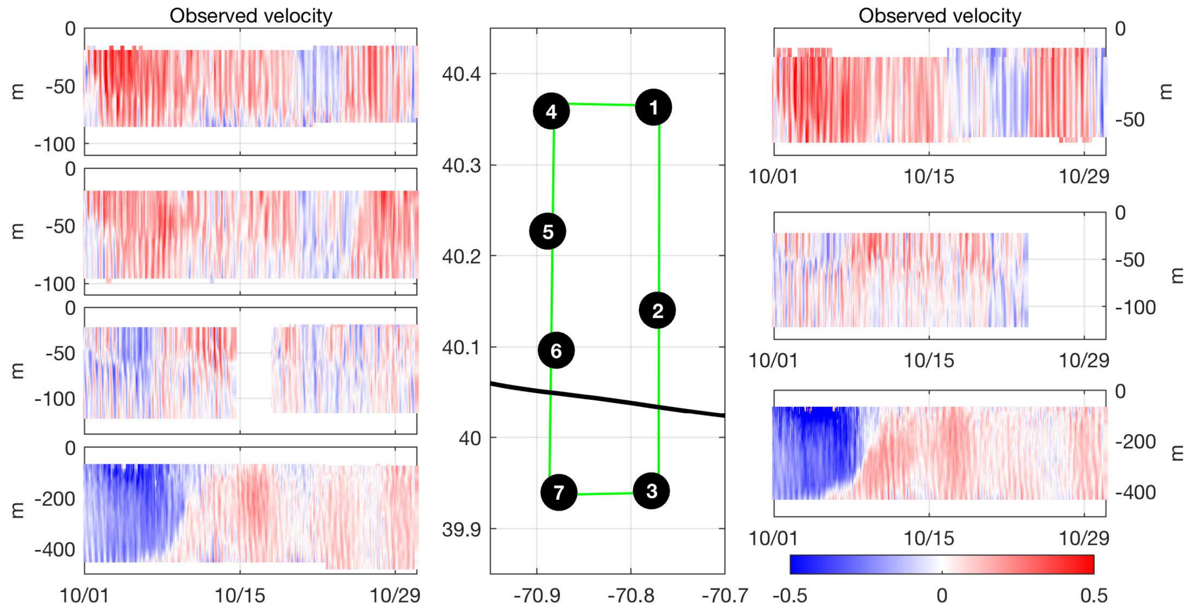

Figure 10: Time series of observed cross-shelf velocity versus depth at the seven Pioneer Array mooring sites during October 2015. In some cases, the color bar is saturated for clarity; positive is onshore flow; the scale is m s^{-1}. The center panel shows the locations of the seven moorings and the portion of the target section crossing the mooring array (black line). The arrangement of the plots echos the mooring positions.

6.3.1 Moorings

Focusing first on the moorings, Fig. 10 shows the cross-shelf component of current as a function of depth and time, as measured at each of the seven Pioneer Array mooring locations during October 2015. While measurements are made only at discrete depths, the velocity data in Fig. 10 have been interpolated in the vertical for clarity. At all mooring locations, strong semi-diurnal tidal currents of up to 0.5 m s^{-1} are very apparent. Superimposed on the tidal flows are lower frequency current reversals with periods upwards of a week or so. The strong offshore flow associated with the low salinity tongue and front formation around 8 October, (*cf.* Fig. 7b) is very evident at moorings 3 and 7 but is waning, and by around 10 October the flow has reversed and proceeds to oscillate weakly with a period of ~7 days.

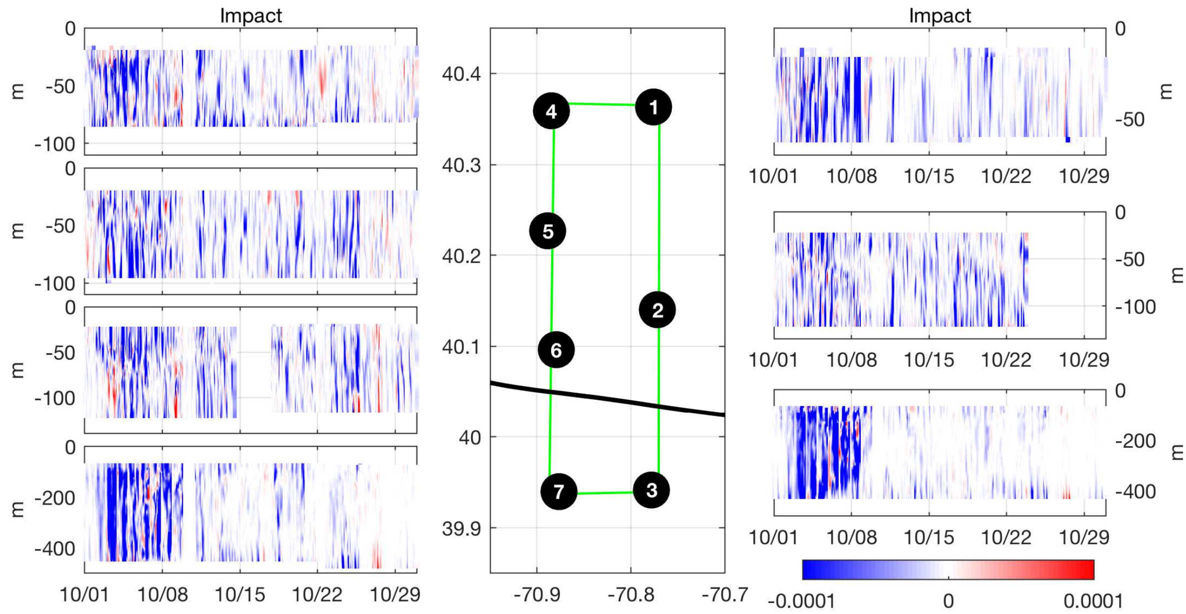

Figure 11: Time series of the impact of cross-shelf velocity versus depth on ΔI_u for G3 at the seven Pioneer Array mooring sites during October 2015. The color bar is saturated in most cases for clarity, and the color bar units are in Sv.

The impact of velocity observations from each mooring location on the G3 cross-shelf volume transport increments ΔI_u is shown in Fig. 11 as a function of depth and time with the same format as Fig. 10. *Negative* impacts indicate that observations at a particular depth and time lead to a *reduction* in the *onshore* transport (or equivalently an *increase* in *offshore* transport), and vice versa for positive impacts. A striking feature of Fig. 11 is that the impact of the mooring velocity measurements is mostly negative, consistent with Fig. 9i, regardless of whether the observed currents are directed offshore or onshore. The largest impacts generally coincide with the peak of the diurnal signal. A particularly striking feature is that for moorings 3 and 7, the impacts are very strongly negative during the formation of the low salinity tongue and salinity front before 10 October, while after that the impact of the measurements from these moorings is much smaller, despite the significant onshore currents (*cf.* Fig. 10).

6.3.2 Gliders

Before looking in detail at the impact of individual Pioneer gliders on the chosen indexes, consider Fig. 12, which shows the RMS vertically integrated impact on ΔI_u of temperature and salinity observations, combined, in each model grid cell during the period 2014-2015 for all three grids. Although the increasing grid resolution going from G1 to G3 is very apparent, the overall spatial distribution of high and low impacts is broadly consistent across the three grids. However, more detailed structures emerge on the higher resolution grids. This is also true for the other indexes (not shown). In particular, hydrographic observations in the vicinity of the target section generally have the largest impact.

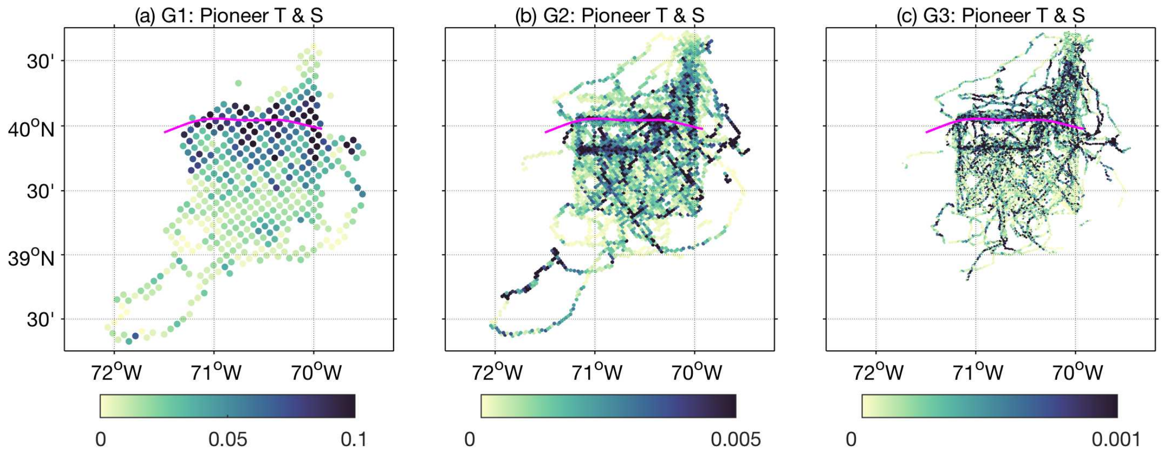

Figure 12: The RMS combined impact of temperature and salinity observations on ΔI_u from all Pioneer gliders during 2014 and 2015 for (a) G1, (b) G2, and (c) G3. The color bars are saturated for clarity, and the units are Sv. The target section is also shown in each case (purple line).

Figures 9a, 9d, and 9g show that during the October 2015 focus period, glider GL380 generally has a significant impact on ΔI_u during the period of frontogenesis in early October. The track of GL380 during this time is shown in Fig. 7c, and during the latter part of the deployment it follows the target section. Figure 13 shows vertical sections of the combined impact on ΔI_u of temperature and salinity observations collected by GL380 for the period 1-15 October for all three grids. For clarity, the impacts are plotted as a function of latitude, longitude and depth from two different 3-dimensional perspectives, and separately as a function of depth and time. The impacts of GL380 on ΔI_u are generally consistent on G2 and G3. For instance, in each case, the impacts are mostly negative, with largest impacts typically associated with near-surface measurements. Positive impacts are mostly found at depth, particularly seaward of the shelf break. In the case of G1, the GL380 impacts are dominated by salinity observations (*cf.* Fig. 9b), and elevated positive impacts are evident after 8 October while the glider is traversing the target section. In all three cases, the outbound leg into deep water during 1-4 October is associated with negative impacts, while the return leg to shallower water 4-7 October is characterized by more positive impacts.

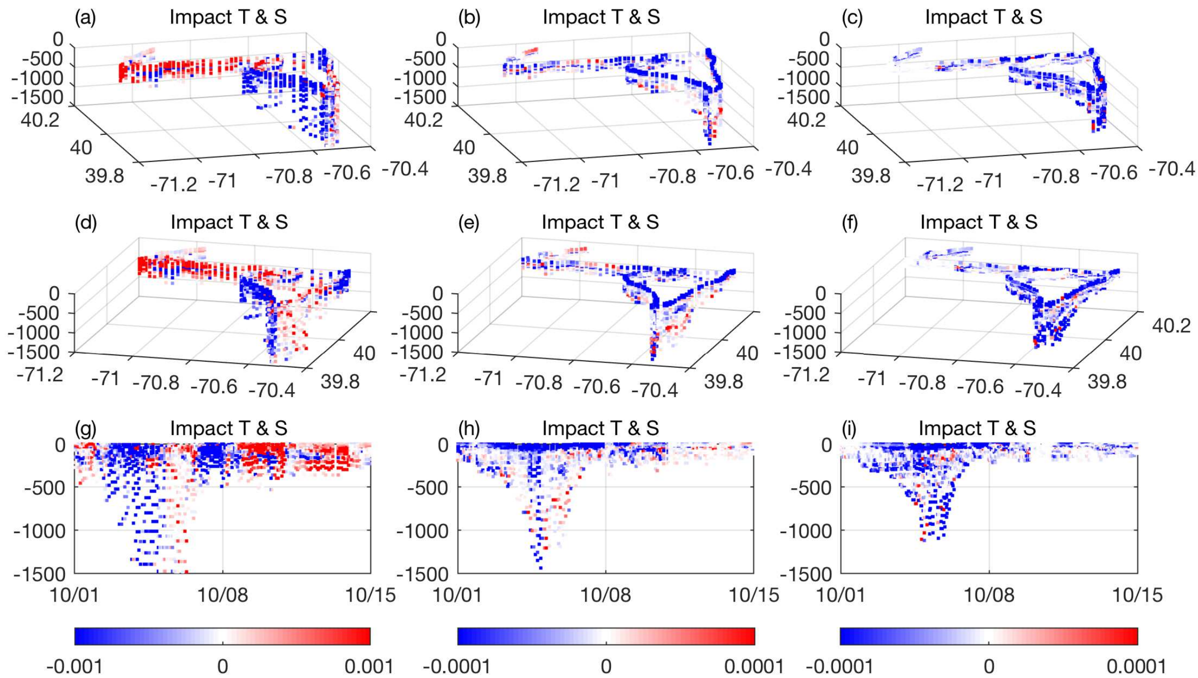

Figure 13: Vertical sections of the combined impact of temperature and salinity observations for Pioneer glider GL380 during the period October 1-15 for (a,d,g) G1, (b,e,h) G2, and (c,f,i) G3. Two different views of the impact versus latitude, longitude, and depth are shown in (a)-(f). The impact versus depth and time is shown in (g)-(i).

Figures 12 and 13 reveal that the impact of individual glider measurements are described by a rich and detailed structure through space and time. Disentangling the full nature of this structure is an ongoing challenge, not only because of the complex flow dynamics in the region but also because the circulation is continuously changing throughout each glider deployment.

6.4 Linear Adjustment Theory

Even though the Rossby number is $O(1)$ (*cf.* Figs. 6c and 7c), the increasing impact of the Pioneer Array mooring velocity observations on the circulation estimates in the vicinity of the target section as grid resolution increases, and the corresponding decline in the impact of hydrographic data, is consistent with linear theory of adjustment. Following Temperton (1973), the stream function ψ_s resulting from the 2-dimensional geostrophic adjustment of an unbalanced circulation estimate derived from data assimilation can be expressed as:

$$\psi_s = \alpha\psi_i + (1-\alpha)f^{-1}\phi_i \qquad (7)$$

where ψ_i and ϕ_i are the initial estimates of the stream function and geopotential height, respectively, and f is the Coriolis parameter. Equation (7) shows that the resulting flow field $u = -\partial\psi_s/\partial y$ and $v = \partial\psi_s/\partial x$ is a linear combination of the initial estimates of the velocity field described by ψ_i and the mass field represented by ϕ_i .The weighting factor α is given by:

$$\alpha = a_e^2(k^2+l^2)/(a_e^2(k^2+l^2)+1) \qquad (8)$$

where k and l are the zonal and meridional wave numbers, respectively, and a_e is the Rossby radius of deformation. Thus equation (8) shows that the relative weighting of the initial velocity field and mass field to the final *balanced* circulation depends on the scale of motion $(k^2 + l^2)^{-1/2}$ compared to the radius of deformation. Specifically, when the length scale of motion is large compared to a_e, then $a_e^2(k^2 + l^2) \rightarrow 0$ and $\alpha \rightarrow 0$, and the final balanced circulation is determined by the initial mass field estimate ϕ_i. Conversely, when the length scale of motion is small compared to a_e, then $a_e^2(k^2 + l^2) \rightarrow \infty$ and $\alpha \rightarrow 1$, and the final balanced circulation is determined by the initial velocity field estimate ψ_i. More generally, this is simply an expression of the partitioning of potential and kinetic energy for the scale of motion considered: large-scale motions are typically dominated by potential energy, so observations of the mass field (*i.e.*, *T*, *S* and or ρ) are most beneficial. In contrast, short-scale motions are usually dominated by kinetic energy, in which case observations of the velocity field are best. However, an important property of (8), as pointed out by Temperton (1973), is that for inhomogeneous flow fields, it is the shortest length scale that determines the weighting factor α. This is illustrated in Fig. 14a, which shows α as a function of $\lambda_x = 2\pi/k$ and $\lambda_y = 2\pi/l$ for $a_e = 20$ km. Figure 14a indicates that if a circulation feature is elongated in one direction, the relative impact of velocity observations and mass field observations is determined by the shortest length scale. When $\alpha \sim 0.5$, this can be thought of as the situation when energy is equipartitioned between potential and kinetic forms, and this situation is shown in Fig. 14a also. As $a_e \rightarrow 0$, the $\alpha = 0.5$ contour collapses toward the λ_x and λ_y axes, exacerbating the dominating influence of the shortest length scale of a flow feature even more.

These ideas are of particular relevance here because, as Fig. 7c shows, the circulation in the vicinity of the shelf-break is dominated by sub-mesoscale features with large horizontal aspect ratios. Thus, it is the cross-frontal and cross-filament length scales that will dictate what type of observations will be most beneficial for recovering the circulation if linear adjustment theory holds. Figure 14b shows how the 1st baroclinic mode radius of deformation $a_e$varies across the G3 domain. In the deep ocean $a_e \sim 20$ km, but it decreases rapidly across the continental slope with $a_e \sim 5$ km or less on the shelf. Most of the sub-mesoscale features in Fig. 7c have cross-front and cross-filament length scales less than the radius of deformation on the shelf, therefore based on (7) and (8), we expect observations of velocity to be more beneficial for recovering the circulation than hydrographic measurements. This is consistent with the findings above. Even though the radius of deformation is in the same range on all three grids, increasing the horizontal resolution going from G1 to G3 leads to the emergence of the sub-mesoscale features that are captured by the Pioneer Array mooring observations.

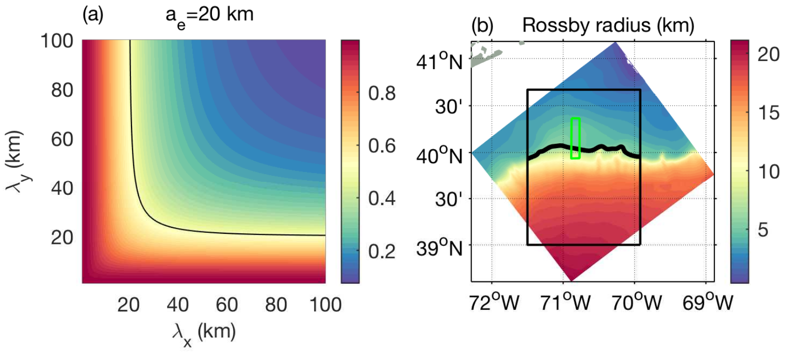

Figure 14: (a) Contours of α versus λ_x and λ_y for a Rossby radius of 20 km. The black contour indicates $\alpha = 0.5$. (b) Variations in the Rossby radius (km) over the G3 domain. The 200 m isobath target section (thick black line), Pioneer glider array (black box), and Pioneer mooring array (green box) are also shown for reference.

These arguments would also account for the relatively low direct impact that HF radar observations have on the G1 circulation estimates, as described by L19. In this case, the horizontal resolution is ~7 km which is larger than the radius of deformation on the shelf, so the scales of motion that will be effectively resolved on G1 will have scales of motion larger than a_e, for which velocity observations will be least effective.

7 Observation Synergy

A summary of the RMS impact of each observation type on all five indexes and across all three grids is shown in Fig. 15 during the October 2015 case study considered in detail in section 6. The overall decrease in the impact of satellite altimetry and *in situ* Pioneer hydrographic observations (from gliders and moorings) going from G1 to G3 is apparent in all indexes, as is the general increase in the impact of velocity observations from the Pioneer moorings. The trend in SST is less clear, where the impact of these data is generally highest on G2 and lowest on G3.

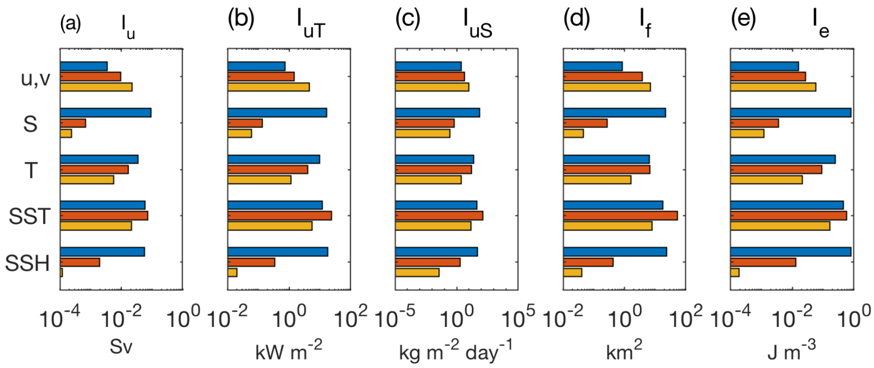

Figure 15: The RMS impact of each observation type for all 4D-Var cycles during October 2015 on (a) I_u, (b) I_{uT}, (c) I_{uS}, (d) I_f, and (e) I_e for G1 (blue), G2 (red) and G3 (orange). Note the $\log_{10}$ scale.

From the summary in Fig. 15, an overall picture begins to emerge about the potential value of the observing system as a whole, and the relative contribution of its components. Such information is, of course, beneficial since it can provide guidance on how ocean observing systems could be most effectively expanded to target specific processes, and how individual assets should perhaps be managed and prioritized. While it is tempting to view the impacts in Fig. 15 as an indication of how each index would change, on average, if each data type was excluded from the 4D-Var analysis, such an interpretation is misleading. This is because the analysis $\boldsymbol{x}^a$ depends not only on the measurement value and location of each observation, but also on the interaction between the observations during the data assimilation process.

The interaction and synergy between different observations and observation platforms can be complicated and difficult to unravel (*e.g.*, Daley, 1991), but can be quantified using a variant of the observation impact methodology described in section 4. Following Moore *et al.* (2011b), suppose that we re-express the analysis equation (1) as:

$$\boldsymbol{x}^a = \boldsymbol{x}^b + \mathcal{K}(\boldsymbol{d}) \qquad (9)$$

where $\mathcal{K}(\boldsymbol{d})$ represents the *entire* data assimilation algorithm expressed as a function of the innovation vector $\boldsymbol{d} = \left(\boldsymbol{y}^o - H(\boldsymbol{x}^b)\right)$. As shown by Moore *et al.* (2011b) and L19, a change $\delta\boldsymbol{y}$ in the observation vector $\boldsymbol{y}^o$ leads to a change δI in the index I which, to 1st-order, can be expressed as:

$$\delta I \approx \delta\boldsymbol{y}^T(\partial\mathcal{K}/\partial\boldsymbol{y}^o)^T(\partial I/\partial\boldsymbol{x})|_{\boldsymbol{x}^b} \qquad (10)$$

where $(\partial\mathcal{K}/\partial\boldsymbol{y}^o)^T$ represents the adjoint of the tangent linearization of the *entire* data assimilation system, and $(\partial I/\partial\boldsymbol{x})|_{\boldsymbol{x}^b}$ represents the derivative of I with respect to $\boldsymbol{x}$ evaluated using the background $\boldsymbol{x}^b$, as in section 4. It is tempting to invoke (1) here and conclude that $(\partial\mathcal{K}/\partial\boldsymbol{y}^o)^T$ is simply the Kalman gain matrix. However, it is important to remember that in any practical implementation of 4D-Var (or any linear data assimilation algorithm) applied to a large dimensional system like that considered here, we can never iterate the system to complete convergence. Thus, the *effective* gain matrix that is used to compute the analysis in (1) will not be the true Kalman gain matrix. Therefore, except in the rare case where 4D-Var is iterated to complete convergence, then in general $(\partial\mathcal{K}/\partial\boldsymbol{y}^o)^T \neq \boldsymbol{K}$.

The ROMS 4D-Var system includes the capability to compute $(\partial\mathcal{K}/\partial\boldsymbol{y}^o)^T$, and from equation (10) it follows that the change in I associated with any change in the observations $\delta\boldsymbol{y}$ can be computed from a *single* application of the adjoint of 4D-Var. Furthermore, Moore *et al.* (2011b) show that if the elements of $\delta\boldsymbol{y}$ are chosen to be -1 times the innovation associated with specific observations, then (10) can be used to compute the change in the index that occurs when these observations are excluded from the 4D-Var analysis. This is a very powerful and efficient tool for performing Observing System Experiments (OSEs) without the need to repeat the costly 4D-Var calculations for each new configuration of the observing system. Since (10) indicates how a given index is influenced by changes in the observations or observing system, it is referred to as "observation sensitivity."

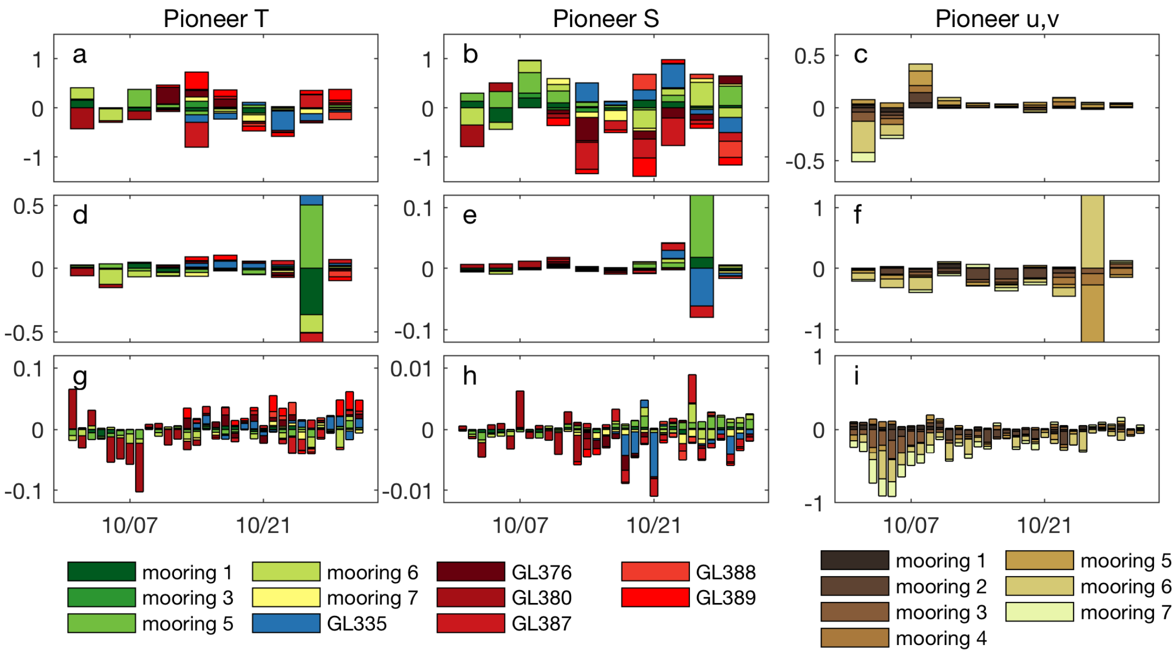

Figure 16: Time series of the change in I_u when Pioneer temperature, salinity, and velocity observations are independently excluded from each 4D-Var data assimilation cycle during October 2015 for (a,b,c) G1, (d,e,f) G2, and (g,h,i) G3. The key for the *T* and *S* platforms is shown to the left, while the key for the velocity observations is shown to the right. In the case of the gliders (GL), shallow gliders are indicated by blue while deep gliders are indicated by different shades of red.

To illustrate this approach, Fig. 16 shows time series of the change in cross-shelf volume transport, δI_u, during the October 2015 case study period when individual components of the glider and mooring arrays are removed from the 4D-Var analysis independently during each data assimilation window. A comparison of Fig. 16 presenting the observation *sensitivity* with Fig. 9 showing observation *impact* reveals that the actual δI_u that results from excluding a particular observing platform from the analysis is very different from what we would infer from the impacts. For example, Fig. 9a shows that during most 4D-Var cycles on G1, the direct impact of glider temperature observations is quite small. Conversely, Fig. 16a indicates that when any individual glider is excluded from the 4D-Var analyses of G1, the changes in cross-shelf transport can be quite significant. A dramatic example is the 3-day assimilation cycle spanning the period 25-27 October on G2. Figures 9d-f show that the transport increment impact during this period is small and positive, and that the impacts of each Pioneer observing platform are generally benign. Conversely, Figs. 16d-f reveal that several of the observing platforms will lead to large increments in transport if omitted from the analysis, and that some assets have largely opposing influences on δI_u.

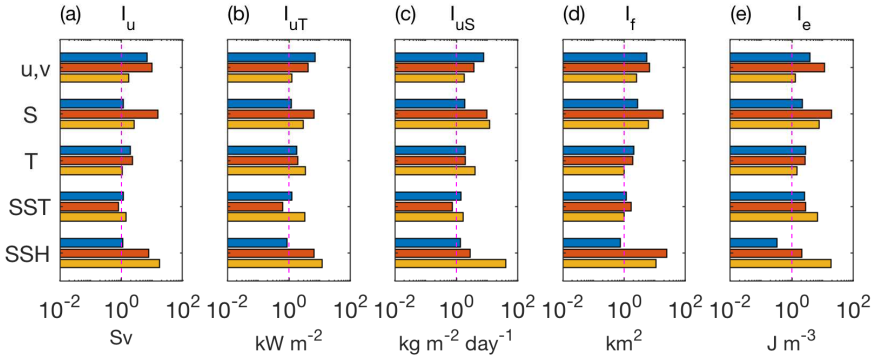

Figure 17: The ratio, b, of the RMS observation sensitivity to the RMS observation impact for all 4D-Var cycles during October 2015 for each observation type for (a) I_u, (b) I_{uT}, (c) I_{uS}, (d) I_f, and (e) I_e for G1 (blue), G2 (red) and G3 (orange). The values of b for *in situ* temperature (*T*), salinity (*S*), and velocity observations (*u,v*) are for the Pioneer Array alone. The red dashed line indicates a ratio of 1. Note the $\log_{10}$ scale.

L19 explored these ideas in some detail with remote sensing observations on G1. They concluded that the seemingly contradictory nature of the results of observation impact and observation sensitivity can be understood in terms of *borrowing strength*, a concept introduced by the Princeton mathematician John Tukey in the 1960s and 70s (Brillinger, 2002). In other words, while a particular observation, y_i say, may not have an especially significant *direct* impact on ΔI, the observation y_i nonetheless provides information that corroborates that from other measurements, and in this way indirectly aids the assimilation process. Therefore, if y_i is excluded from the 4D-Var analysis, the corroborating information that it provides will be lost, leading to a much larger change in I than might otherwise be expected based on an observation impact calculation alone. Thus, in this way, other observations *borrow strength* from y_i. L19 argue that the degree to which different components of the observing system borrow strength from each other can be quantified using the ratio of the observation sensitivity to the observation impact.

Drawing on this idea, Fig. 17 shows the ratio, b, of the RMS observation sensitivity to the RMS observation impact for all indexes, across all three grids, and for all measurement types averaged over all 4D-Var cycles during October 2015. This ratio is a measure of the average change that *actually* occurs in each index when an observation is excluded from all 4D-Var analyses and that which might be *expected* to occur based on the observation impact alone. A value of $b = 1$, therefore, indicates that, on average, the sensitivity and impact calculations predict similar changes in a given index if observations of this type are excluded from each 4D-Var cycle. Conversely, values of $b > 1$ ($b < 1$) indicate that the actual change in I will be larger (smaller) than expected based on the observation impact calculations. Therefore, departures of b from a value of one can be viewed as an indicator of the level of borrowing strength. Note that the ratios shown in Fig. 17 for *in situ* temperature, salinity, and velocity data are for observations collected from the Pioneer Array only.

Several striking features appear in Fig. 17. First, in all but a few cases, $b > 1$ on all three grids indicating that all components of the observing system are borrowing strength from one another. Only in the case of satellite SST and altimetry do we see instances of $b < 1$ for some of the indexes on G2 and G3. Second, in the case of velocity observations, b is large on G1 (~10), indicating that while Fig. 15 shows a relatively modest direct impact of these data on all indexes, the actual change that will occur in each I will be much larger than the impact implies if velocity observations are excluded from the 4D-Var analysis. The values of b for velocity observations decrease for the transport indexes (Figs. 17a-c) moving from G1 to G3, in contrast to the increasing impact of these data (Figs. 15a-c). Therefore, as the mooring velocity observations exert more of a direct influence on the sub-mesoscale circulation environment, the degree to which they *lend* strength to the other components of the observing system lessens. However, the distribution of information amongst the seven different Pioneer Array moorings implied by the observation impact and observation sensitivity calculations is different, as seen by comparing Fig. 9i and Fig. 16i. For I_f and I_e, Fig. 17 shows that the ratio b increases for velocity observations going from G1 to G2, indicating that the indirect influence of these observations is enhanced further. Finally, while b increases substantially between G1 and G3 for some observations, this can be accompanied by a significant decrease in the direct observation impact. For example, Fig. 17 shows that b associated with satellite altimetry increases by ~1-2 orders of magnitude between G1 and G3. However, Fig. 15 reveals that there is a corresponding reduction in the direct impact of these data on each index. Therefore, while the volume of altimetry observations diminishes considerably between G1 to G3 (due to the reduction in the size of the geographical domain), the few altimeters passes that cross G3 during October 2015 do, nonetheless, *lend* considerable strength to the other observing platforms.

Figures 15 and 17 highlight the complex nature of the flow of observational information through the data assimilation system, and efforts are ongoing to understand the mechanics of this process further.

8 Analysis Error Estimates

Having established the impact that different components of the observing system have on estimates of the cross-shelf exchange, it is important also to quantify the degree to which the observations contribute to the expected uncertainties in each of the target indexes, I. The expected analysis error covariance, $\boldsymbol{A}$, of $\boldsymbol{x}^a$ in (1) is given by $\boldsymbol{A} = (\boldsymbol{I} - \boldsymbol{KH})\boldsymbol{B}(\boldsymbol{I} - \boldsymbol{KH})^T + \boldsymbol{KRK}^T$ (Daley, 1991). In practice, however, $\boldsymbol{A}$ is difficult to evaluate for 4D-Var systems and typically requires a Monte Carlo approach (Bennett, 2002; Ngodock *et al.*, 2020) or a low-rank approximation (Fisher and Courtier, 1995). Moore *et al.* (2012) considered an alternative adjoint approach based on (10). Specifically, Moore *et al.* (2012) examined an infinite ensemble of δI based on different realizations of perturbations to the innovations $\delta\boldsymbol{d} = (\delta\boldsymbol{y} - \boldsymbol{H}\delta\boldsymbol{x}^b)$ where $\delta\boldsymbol{x}^b$ are perturbations in the background. If $\delta\boldsymbol{y}$ and $\delta\boldsymbol{x}^b$ are drawn from normal distributions with zero mean and covariance $\boldsymbol{R}$ and $\boldsymbol{B}$ respectively, then, for a single outer-loop, it can be shown that, to 1st-order, $\boldsymbol{A}$ can be approximated as:

$$\boldsymbol{A} = (\boldsymbol{I} - (\partial\mathcal{K}/\partial\boldsymbol{d})\boldsymbol{H})\boldsymbol{B}(\boldsymbol{I} - (\partial\mathcal{K}/\partial\boldsymbol{d})\boldsymbol{H})^T + (\partial\mathcal{K}/\partial\boldsymbol{d})\boldsymbol{R}(\partial\mathcal{K}/\partial\boldsymbol{d})^T \quad (11)$$

where $(\partial\mathcal{K}/\partial\boldsymbol{d})^T \equiv (\partial\mathcal{K}/\partial\boldsymbol{y})^T$ is the adjoint of the 4D-Var system introduced in section 7. The expected error variance in any index $I(\boldsymbol{x}^a)$ is then given by $\sigma_I^2 = (\partial I/\partial\boldsymbol{x})|_{\boldsymbol{x}^b}^T\boldsymbol{A}(\partial I/\partial\boldsymbol{x})|_{\boldsymbol{x}^b}$.

Using (11), σ_I^2 can be expressed as $\sigma_I^2 = \sigma_B^2 - \sigma_C^2$ where:

(a) $\sigma_B^2 = (\partial I/\partial \boldsymbol{x})|_{\boldsymbol{x}^b}^T \boldsymbol{B}(\partial I/\partial \boldsymbol{x})|_{\boldsymbol{x}^b}$ is the background error variance of $I(\boldsymbol{x}^b)$ and;

(b) $\sigma_C^2 = \boldsymbol{g}^T\left(2\boldsymbol{HB}(\partial I/\partial \boldsymbol{x})|_{\boldsymbol{x}^b} - \boldsymbol{HBH}^T\boldsymbol{g} - \boldsymbol{Rg}\right)$ is the expected reduction in the error variance due to assimilating the observations, where $\boldsymbol{g} = (\partial \mathcal{K}/\partial \boldsymbol{d})^T(\partial I/\partial \boldsymbol{x})|_{\boldsymbol{x}^b}$ is the result of the observation sensitivity calculations in section 7.

The correction term σ_C^2 takes the form of a dot-product of two vectors in observation-space, so the contribution of each observing platform to the expected reduction σ_C^2 in the background error σ_B^2 can be computed.

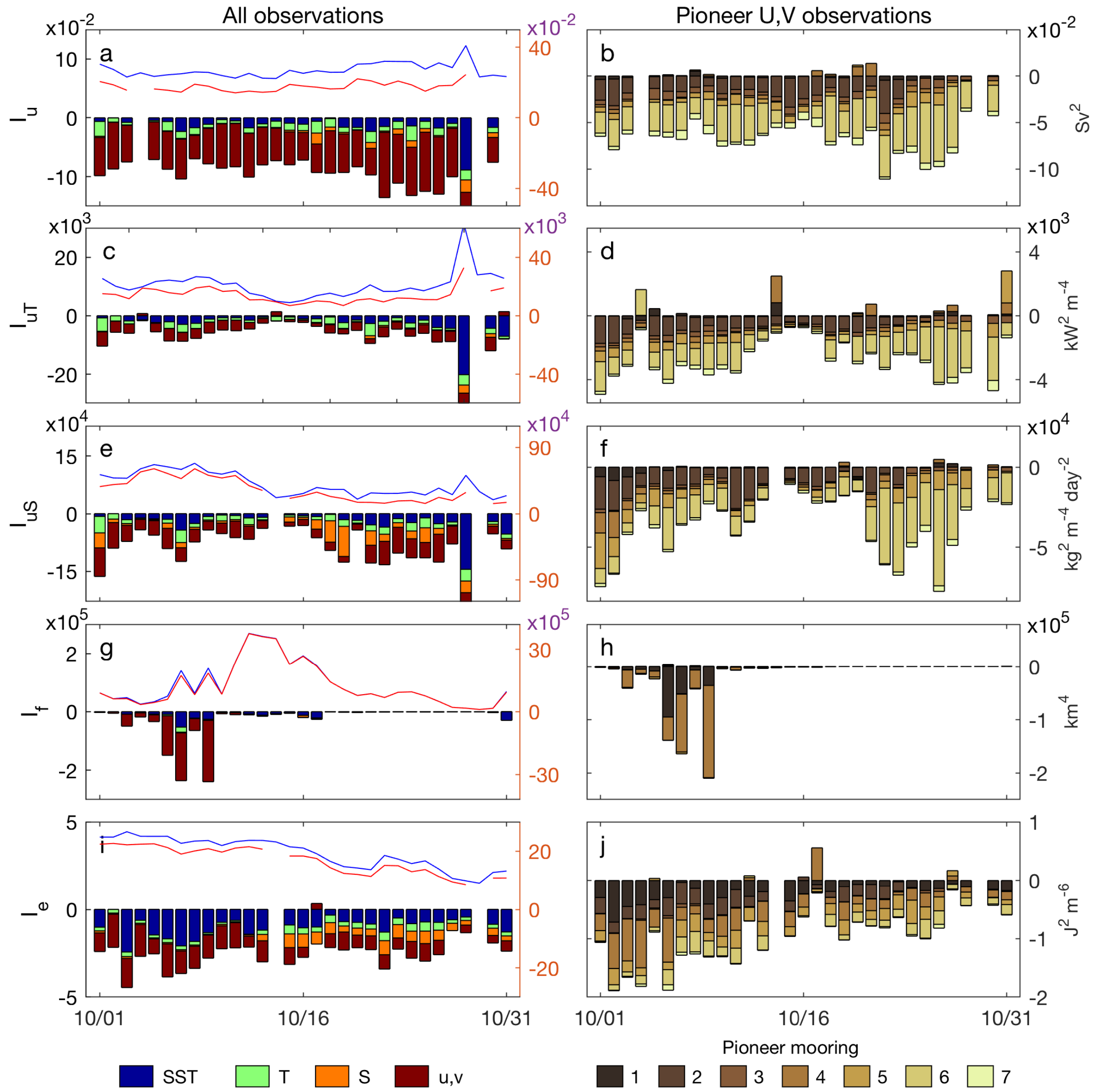

Figure 18: Time series of $-\sigma_C^2$ for each index on G3 during October 2015 for (a) I_u, (c) I_{uT}, (e) I_{uS}, (g) I_f, and (i) I_e. The contribution of each type of observation to $-\sigma_C^2$ is indicated in each case. Since the contribution of SSH is negligible, it is not shown. The scale for $-\sigma_C^2$ is shown on the left. Also shown are the time series of the background

error variance σ_B^2 (blue line) and the expected analysis error variance σ_I^2 (red line). The scale for σ_B^2 and σ_I^2 is shown on the right. Time series of the contributions to $-\sigma_C^2$ of velocity observations from each of the Pioneer moorings are shown for (b) I_u, (d) I_{uT}, (f) I_{uS}, (h) I_f, and (j) I_e. All calculations are based on the 1st outer-loop. Missing values are associated with a few cycles where the approximation described by (11) breaks down, possibly because higher-order terms are required (*e.g.*, Errico, 2007).

Figure 18 shows time series of σ_C^2 for each index from the G3 4D-Var analyses during October 2015 and the contribution of each type of observation. Also shown for reference are time series of the background error variance σ_B^2 associated with $I(\boldsymbol{x}^b)$ and the expected analysis error variance σ_I^2. These statistics were computed for the 1st outer-loop alone since, as shown in Part I, the largest increments typically occur during at this time. It is possible to calculate the expected analysis errors for the 2nd outer-loop also, but such a computation is complicated and costly, as shown by Moore and Arango (2020). It is important to appreciate that $\boldsymbol{A}$ will only be the true analysis error covariance matrix *if* both $\boldsymbol{B}$ and $\boldsymbol{R}$ are the true background and observation error covariance matrices. Since this is never the case, we should not place too literal of an interpretation on $\boldsymbol{A}$. Nonetheless, the reduction $\sigma_C^2 = \sigma_B^2 - \sigma_I^2$ in the background error variance is a useful guide for exploring the relative degree to which different observation platforms reduce uncertainties in each index.

For the majority of indexes, Fig. 18 indicates that there is a modest reduction in the expected analysis error due to assimilating the observations. The exception is I_f for which there is no discernable decrease of the expected uncertainty in the position of the MAB foot front due to data assimilation except during the 2nd week of Oct. Figure 18 also shows that *in situ* observations from the Pioneer Array, in combination, contribute most to σ_C^2, although during some cycles, SST errors are important too. Given the focus in sections 6 and 7 on velocity observations from the Pioneer Array moorings, Fig. 18 also shows the contribution to σ_C^2 of these data alone from each mooring. For the transport indexes (*i.e.*, I_u, I_{uT}, and I_{uS}), observations from the shelf-break mooring 6 (*cf.* Fig. 2) contribute most to expected errors in each index. On the other hand, for I_e, the contributions to σ_C^2 from the different moorings are generally more evenly distributed. In the case of I_f, there are a few cycles during the first two weeks where moorings 1 and 4 have the largest influence on σ_I^2, but as noted above, σ_C^2 is very small for this index. It is also interesting to note that for some indexes, there are opposing influences of different moorings on σ_I^2 (*e.g.*, for I_{uT} in Fig. 18d).

Figure 18 provides a direct and quantitative measure of the role that each type of observation and observing platform plays in controlling the *expected* efficacy of the 4D-Var circulation estimates, the particular focus here being on the position and strength of the MAB front, and environmental factors, such as stratification, that control cross-shelf exchange.

9 Summary and Conclusions

This study is an extension of Part I in which observations from remote sensing and *in situ* platforms were assimilated into a configuration of ROMS comprising three-levels of telescoping nested grids centered on the Mid-Atlantic Bight. In particular, the impact of the different components of the MAB and Gulf of Maine observing systems on analyses of cross-shelf exchange was evaluated and assessed. A critical element in the MAB observing system is the

NSF OOI Pioneer Array. In this Part II, our focus has been on the impact of the observations from the Pioneer Array on 4D-Var estimates of cross-shelf exchange.

The impact of different types of observations was found to change across the three grids. As discussed in Part I, the impact of the observations on each grid depends on several factors that include: (a) the number and distribution of the observations; (b) the background circulation, which, of course, depends on the resolution of the grid; (c) the background error covariance, $\boldsymbol{B}$; and (d) the observation error covariance, $\boldsymbol{R}$. Differences in resolution, limitations of the assimilation system, and operational constraints dictate that the parameters used to compute $\boldsymbol{B}$ and $\boldsymbol{R}$ should vary across the three grids. Therefore, some of the changes in the impact of the observations across the three grids can be attributed to different *a priori* choices of error statistics. With this in mind, it was found that temperature observations from the Pioneer gliders typically have a significant impact on the cross-shelf exchange on all three grids, which is partly a reflection of similar levels of uncertainty assumed for the combined influences of instrument error and errors of representativeness. Salinity observations, on the other hand, are more impactful on G1 than on G2 and G3. This is partly because the errors assigned to salinity observations are smallest on G1 but, as described in Part I, were subsequently reduced on G2 and G3 in accordance with *a posteriori* analysis of the innovation statistics. However, another factor that controls the impact of salinity (and indeed temperature) observations is the ensuing geostrophic adjustment process that acts to re-establish a dynamic balance following the introduction of observations by the data assimilation.

The impact of velocity observations from the Pioneer Array moorings was found to increase with increasing resolution. The increase in impact from G1 to G2 is partly associated with a reduction in the observation errors assigned to these data on G2, again in accordance with the *a posteriori* innovation statistics as described in Part I. A further increase in impact of velocity observations from the moorings was found on G3 compared to G2 which in this case is associated with the increase in horizontal resolution and the emergence of significant sub-mesoscale variability.

To explore the impact of the observations on data assimilation spanning the different but connected dynamical circulation regimes captured by the three nested grids, we focused attention on a 4-week window in 2015 during the interaction of a Gulf Stream ring with the continental shelf, as captured by the 4D-Var analyses of G1. On G2 and G3, this same period is characterized by sub-mesoscale frontogenesis in the vicinity of the Pioneer Array, which appears to be initiated by the flow field that develops where several mesoscale eddies come together. During this event, velocity observations from the Pioneer mooring array exert considerable influence on the G2 and G3 circulation estimates, much more so than hydrographic measurements. Even though the local Rossby number of the circulation is $O(1)$, these findings are consistent with the linear theory of geostrophic adjustment, also invoked in the early days of meteorological data assimilation to explain the relative effectiveness of wind and pressure observations for recovering the atmospheric state.

The synergy between the different types of observations during the 4D-Var estimation process was also explored by exploiting the complementary information provided by the observation impact and observation sensitivity calculations. Observation impact quantifies the actual contribution of each observation to the 4D-Var analysis, while observation sensitivity dictates how the analysis must change if a specific observation is excluded from the 4D-Var procedure. The ratio, b, of the observation sensitivity and observation impact can be used as an indicator of *borrowing strength*, whereby data from, say, platform A for which $b > 1$ provides important corroborating information that supports information gathered by other components of the observing system, even if platform A, *per se*, has a relatively small directly measurable impact on the circulation.

Finally, we examined the contribution that each observing platform has on the expected uncertainty in the 4D-Var estimates of cross-shelf exchange on G3. Specifically, the difference between the expected error variance of the 4D-Var analysis and the error variance of the background can be partitioned into the contribution associated with each observation. For most indexes, the Pioneer Array dominates the reduction in uncertainty of the circulation estimates, and much of the time velocity observations from the Pioneer moorings are the major contributor. This again highlights the critical role that direct measurements of ocean currents play in our ability to estimate, and potentially forecast the sub-mesoscale environment.

This study demonstrates the extraordinary level of detailed information that can be teased from the application of the ideas that underpin the notion of observation impact and observation sensitivity. We have only just begun to scratch the surface here. Clearly though, routine monitoring of such information for carefully selected circulation indexes holds promise to provide an efficient and highly effective way of monitoring the veracity of not only the circulation estimates themselves but also the performance and efficacy of each component of the observing system. Such information will surely be useful for quantifying the socio-economic impacts of, in this case, the IOOS observing system, and for efficient management of the existing observing system. Other potential spin-offs of the work presented here, which we are actively pursuing, include repurposing of the 4D-Var adjoint calculations of section 8 to determine how the expected analysis error covariance will change when different components of the observing system are withheld, and observing system design to augment existing observing systems, such as the Pioneer Array and those maintained by IOOS.

Acknowledgements

This work was supported by grants from the National Science Foundation (OCE-1459665 and OCE-1459646), NASA (NNX17AH58G) and NOAA (NA16NOS0120020). Pioneer Array data were obtained from the NSF Ocean Observatories Initiative Data Portal http://ooinet.oceanobservatories.org.

References

Andersson, E., Järvinen, H., 1999. Variational quality control. *Q. J. R. Meteorol. Soc*. **125**, 679-722.

Beardsley, R.C., Chapman, D.C., Brink, K.H., Ramp, S.R., Schlitz, R., 1985. The Nantucket Shoals Experiment (NSFE79), I, A basic description of the current and temperature variability. *J. Phys. Oceanogr.*, **15**, 713-748.

Bennett, A.F., 2002. Inverse Modeling of the Ocean and Atmosphere. Cambridge University Press, 234pp.

Boyer, T., Antonov, J., Baranova, O., Garcia, H., Johnson, D., Locarnini, R., Mishonov, A., OBrien, T., Seidov, D., Smolyar, I., Zweng, M., 2009. World ocean database 2009. In: Levitus, S. (Ed.), NOAA Atlas NESDIS 66, 216pp.

Brillinger, D., 2002. John W. Tukey: his life and professional contributions. *Ann. Stat.* **30**, 1535–1575.

Courtier, P., 1997. Dual formulation of four-dimensional variational assimilation. *Q. J. R. Meteorol. Soc.*, **123**, 2449-2461.

Daley, R., 1991. Atmospheric Data Analysis. Cambridge University Press, 457pp.

Desroziers, G., Berre, L., Chapnik, B., Poli, P., 2005. Diagnosis of observation, background and analysis-error statistics in observation space. *Q. J. R. Meteorol. Soc*. **131**, 3385-3396.

Errico, R.M., 2007. Interpretations of an adjoint-derived observational impact measure. *Tellus* **59A**, 273-276.

Fleming, N., 2016. Seasonal and spatial variability in temperature, salinity and circulation of the Middle Atlantic Bight. PhD thesis, 336pp.

Fisher, M., Courtier, P., 1995. Estimating the covariance matrices of analysis and forecast error in variational data assimilation. *ECMWF Tech. Memo*. **220**, 28pp.

Fujii, Y., Rémy, E., Zuo, H., Oke, P., Haliwell, G., Gasparin, F., Benkiran, M., Loose, N., Cummings, J., Xie, J., Xue, Y., Masuda, S., Simith, G.C., Balmaseda, M., Germineaud, C., Lea, D.J., Larnicol, G., Bertino, L., Bonaduce, A., Brasseur, P., Donlon, C., Heimbach, P., Kim, Y., Kourafalou, V., Le Traon, P., Martin, M., Paturi, S., Tranchant, B., and Usui, N., 2019. Observing System Evaluation Based on Ocean Data Assimilation and Prediction Systems: On-Going Challenges and a Future Vision for Designing and Supporting Ocean Observational Networks. *Frontiers in Marine Science*, https://doi.org/10.3389/fmars.2019.00417.

Gawarkiewicz, G., Todd, R., Zhang, W., Partida, J., Gangopadhyay, A., Monim, M.U.H., Fratantoni, P., Malik, A.M., Dent, M., 2018. The changing nature of shelf-break exchange revealed by the OOI Pioneer Array. *Oceanography* **31**, 60–90.

Gürol, S., Weaver, A., Moore, A., Piacentini, A., Arango, H., Gratton, S., 2014. B-preconditioned minimization algorithms for variational data assimilation with the dual formulation. *Quart. J. R. Meteorol. Soc.* **140**, 539–556.

Langland, R., Baker, N., 2004. Estimation of observation impact using the NRL atmospheric variational data assimilation adjoint system. *Tellus* **56A**, 109–201.

Lellouche, J.-M., Greiner, E., Le Galloudec, O., Garric, G., Regnier, C., Drévillon, M., Benkiran, M., Testut, C.-E., Bourdallé-Badie, R., Gasparin, F., Hernandez, O., Levier, B., Drillet, Y., Remy, E., and Le Traon, P.-Y., 2018. Recent updates to the Copernicus Marine Service global ocean monitoring and forecasting real-time 1/12° high-resolution system, *Ocean Sci*., **14**, 1093–1126.

Levin, J., Arango, H.G., Laughlin, B., Wilkin, J., Moore, A.M., 2019. The impact of remote sensing observations on cross-shelf transport estimates from 4D-Var analyses of the Mid-Atlantic Bight. *Advances in Space Research*, https://doi.org/10.1016/j.asr.2019.09.012

Levin, J., Arango, H.G., Laughlin, B., Wilkin, J., Moore, A.M., 2020. Observation Impacts on the Mid-Atlantic Bight Front and Cross-Shelf Transport in 4D-Var Ocean State Estimates: Part I – Multiplatform Analysis.

Linder, C., Gawarkiewicz, G., 1998. A climatology of the shelf break front in the Middle Atlantic Bight. *J. Geophys. Res.* **102**, 18405–18423.

Moore, A.M., Arango, H.G., Broquet, G., Edwards, C.A., Veneziani, M., Foley, B.P.D., Doyle, J., Costa, D., Robinson, P., 2011a. The Regional Ocean Modeling System (ROMS) 4-dimensional variational data assimilation systems. Part I: system overview and formulation. *Prog. Oceanogr*. **91**, 34-49.

Moore, A.,M. Arango, H.G., Broquet, G., Edwards, C., Veneziani, M., Foley, B.P.D., Doyle, J., Costa, D., Robinson, P., 2011b. The Regional Ocean Modeling System (ROMS) 4-dimensional variational data assimilation systems. Part III: observation impact and observation sensitivity in the California Current System. *Prog. Oceanogr.* **91**, 74–94.

Moore, A.M., Arango, H.G., Broquet, G., 2012. Analysis and forecast error variance estimates derived from the adjoint of 4D-Var. *Mon. Wea. Rev.* **140**, 3183-3203.

Moore, A.M., Arango, H.G., 2020. On the behavior of ocean analysis and forecast error covariance in the presence of baroclinic instability. *Ocean Modelling*, submitted.

Ngodock, H., Souopgui, I., Carrier, M., Smith, S., Osborne, J., Addezio, D., 2020. An ensemble of perturbed analyses to approximate the analysis error covariance in 4dvar. *Tellus* A: *Dynamic Meteorology and Oceanography*, **72:1**, 1-12, DOI:10.1080/16000870.2020.1771069.

Oke, P.R., Larnicol, G., Fujii, Y., Smith, G.C., Lea, D.J., Guinehut, S., Remy, E., Balmaseda, M.A., Rykova, T., Surcel-Colan, D., Martin, M.J., Sellar, A.A., Mulet, S., Turpin, V., 2015a. Assessing the impact of observations on ocean forecasts and reanalyses: Part 1, global studies. *J. Oper. Oceanogr*. 8**,** s49–s62.

Oke, P.R., Larnicol, G., Jones, E.M., Kourafalou, V., Sperrevik, A.K., Carse, F., Tanajura, C.A.S., Mourre, B., Tonani, M., Brassington, G.B., Le Henaff, M., Halliwell, G.R., Atlas, R., Moore, A.M., Edwards, C.A., Martin, M.J., Sellar, A.A., Alvarez, A., De Mey, P., Iskandarani, M., 2015b. Assessing the impact of observations on ocean forecasts and reanalyses: Part 2, regional applications. *J. Oper. Oceanogr*. **8**, s63–s79.

Simpson, J.H., Bowers, D., 1981. Models of stratification and frontal movement in shelf seas. *Deep Sea Research* **28A**, 727-738.

Temperton, C., 1973. Some experiments in dynamic initialization for a simple primitive equation model. *Quart. J. R. Meteorol. Soc.* **99**, 303-319.

Trémolet, Y., 2008. Computation of observation sensitivity and observation impact in incremental variational data assimilation. *Tellus* **60A**, 964–978.

Weaver, A., Courtier, P., 2001. Correlation modelling on the sphere using a generalized diffusion equation. *Quart. J. R. Meteorol. Soc.* **127**, 1815–1846.